

Supplementary Materials for
**Unraveling quantum coherences mediating primary charge transfer
processes in photosystem II reaction center**

Ajay Jha *et al.*

Corresponding author: Hong-Guang Duan, duanhongguang@nbu.edu.cn;
Michael Thorwart, michael.thorwart@physik.uni-hamburg.de;
R. J. Dwayne Miller, dmiller@lphys.chem.utoronto.ca

Sci. Adv. **10**, eadk1312 (2024)
DOI: 10.1126/sciadv.adk1312

This PDF file includes:

Supplementary Text
Figs. S1 to S24
Tables S1 and S2
References

Supplementary Text

In this supplementary text, we discuss the measurements of the lifetimes of the electronic dephasing and describe the global fitting approach. We then present the two-dimensional (2D) decay-associated spectra (DAS) of the PSII reaction center. We also show the transformation from the site to the exciton basis representation and resolve the occupation dynamics of each pigment in the exciton basis. The Tukey window Fourier transformation is reviewed as well. Moreover, the detailed fitting procedure, the resolved electronic and vibrational coherence and the associated lifetimes are presented in the subsequent section. For the analysis of the 2D spectra, we also describe the exciton model and the refined fitting of the parameters of the PSII reaction center. Then, detailed calculations of the response function and the 2D electronic spectra are presented in the following. In addition, we describe the modified Redfield quantum master equation and the quadiabatic propagator path integral method in the last section.

I. TIME CONSTANT OF THE ELECTRONIC DEPHASING MEASURED FROM 2D SPECTRA

In this section, we investigate the time constant of the electronic dephasing extracted from the measured 2D electronic spectra. In Fig. S1(a), we show the 2D electronic spectrum (total and real part) and the anti-diagonal cut (black solid line). The magnitude along the probing frequency is plotted as red solid line in Fig. S1(b). We resolve the bandwidth of the main peak and analyze it by a fit to a Lorentzian line shape function. The fitting is performed by the Curve Fitting Toolbox (Matlab 2021(b)) and the resulting data are shown as blue dashed line in Fig. S1(b). We resolve the time constant of the electronic dephasing as 165 fs. It manifests the timescale of optical dephasing between the electronic ground and the excited states in the PSII reaction center.

II. GLOBAL FITTING APPROACH AND RESOLVED COMPONENTS OF THE DAS

Here, we briefly review the global fitting approach. A detailed account is found in Ref. 33. First, we construct a series of 2D electronic spectra of the PSII reaction center and fit the kinetics by several amplitude maps $A_i(\omega_\tau, \omega_t)$ with exponential decay components characterized by τ_i , i.e.,

$$S(\omega_\tau, T, \omega_t) = \sum_i A_i(\omega_\tau, \omega_t) \exp(-T/\tau_i), \quad (\text{S1})$$

where $A_i(\omega_\tau, \omega_t)$ is the decay associated spectrum (DAS) with the decay time τ_i . We extend the probing window to 500 ps in order to capture the process of secondary charge transfer. The obtained results are shown in Fig. S2. The data analysis yields 6 components with the decay time constants of 27 fs, 700 fs, 4.9 ps, 27 ps, 104 ps and infinity, respectively. The fastest component with the timescale of 27 fs mainly stems from the peak broadening and the pulse-overlap effect. The second DAS component shows clear evidence of down-hill population transfer. The positive main peak and the negative cross peaks indicate the energy and CT dynamics occurring on the timescale of 700

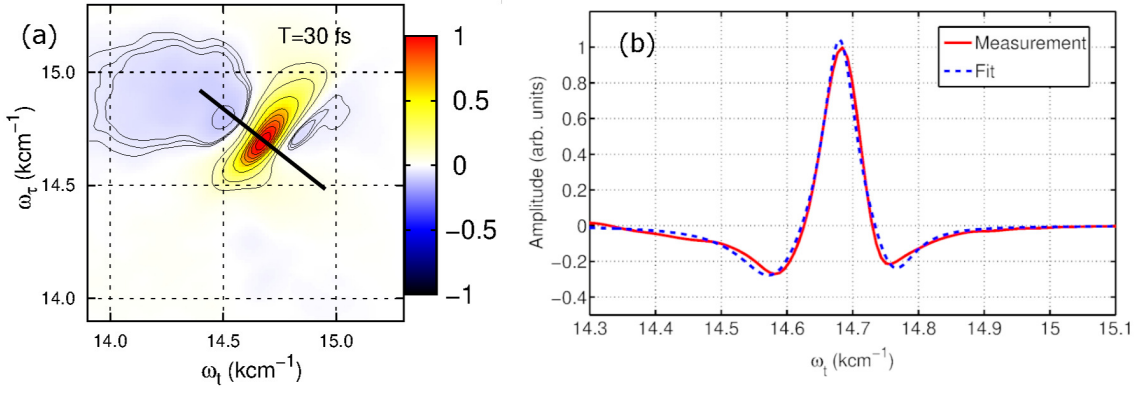


FIG. S1. (a) Anti-diagonal cut in 2D electronic spectrum at 30 fs (real total part). (b) Measured lineshape of the anti-diagonal profile and estimate of the lifetime of the electronic dephasing by a fitted Lorentzian lineshape function. The obtained lifetime of electronic dephasing is 165 fs.

fs. The detailed description of this component is presented in the main text. More importantly, we note that the uncovered electronic quantum coherence in the PSII reaction center persists for 600 fs (with a lifetime of 177 fs), which coincides with the timescale of the 700 fs-component. We thus conclude that the DAS component associated with the decay time of 700 fs strongly relates to the coherent energy transfer in the PSII reaction center. In addition, we also resolve the DAS components with timescales of 4.9 ps, 27 ps and 104 ps, respectively. The growth of the transfer times manifests the multiple pathways of the secondary charge transfers in the PSII reaction center. Moreover, the “infinity” component indicates the energy levels of the lowest excitonic states in the PSII reaction center.

III. TUKEY WINDOW FOURIER TRANSFORM

In this section, we provide the details of the Fourier transform with the Tukey window. To suppress the high-frequency jitters, Fourier filtering in the frequency domain is employed to isolate each of these regions of interest by a Tukey window of the form

$$\omega(n) = \begin{cases} 1, & 0 \leq |n| \leq \alpha \frac{N}{2}, \\ \frac{1}{2} \left(1 + \cos \left[\frac{\pi(n - \alpha \frac{N}{2})}{(1 - \alpha) \frac{N}{2}} \right] \right), & \alpha \frac{N}{2} \leq |n| \leq \frac{N}{2}, \end{cases} \quad (\text{S2})$$

which, due to the flat top, conserves the amplitudes of the Fourier components of interest over a frequency range larger than a cosine or a Gaussian window, while it still limits the artifacts arising from a pure bandpass filter. In this work, we use the Tukey window with $\alpha = 1/5$ and a Fourier bandpass filter with $\leq 700 \text{ cm}^{-1}$.

IV. FITTING PROCEDURE AND RESOLVED ELECTRONIC AND VIBRATIONAL COHERENCES

In this section, we describe the procedure to treat the residuals and to disentangle the electronic and vibrational coherences using the Curve Fitting Toolbox in Matlab 2021(b). First, we extract the time-resolved traces starting from the raw data of the rephasing part of the 2D electronic spectra. The results are shown as black square dots in Fig. S3. The subsequent treatments by the Tukey window Fourier transform yield to the red solid lines in Fig. S3(a) to (c). The excellent quality of the fits of the raw data and the refined traces demonstrates the suitability of this data treatment by the Tukey window Fourier transform. By this, we obtain refined data of the time-resolved kinetics. We further employ the exponential functions to fit the kinetics and obtain the residuals after subtracting the kinetics. The quality of the fitting is indicated by the magenta dashed lines in Fig. S3(a), (b) and (c). The resulting residuals are plotted as blue solid lines.

The obtained Fourier-filtered traces are uploaded into the curve fitting toolbox in Matlab 2021(b). The fitting function is given as

$$\sum_i^N A_i \exp(-T/\tau_i) \sin(\omega_i T + \phi_i). \quad (\text{S3})$$

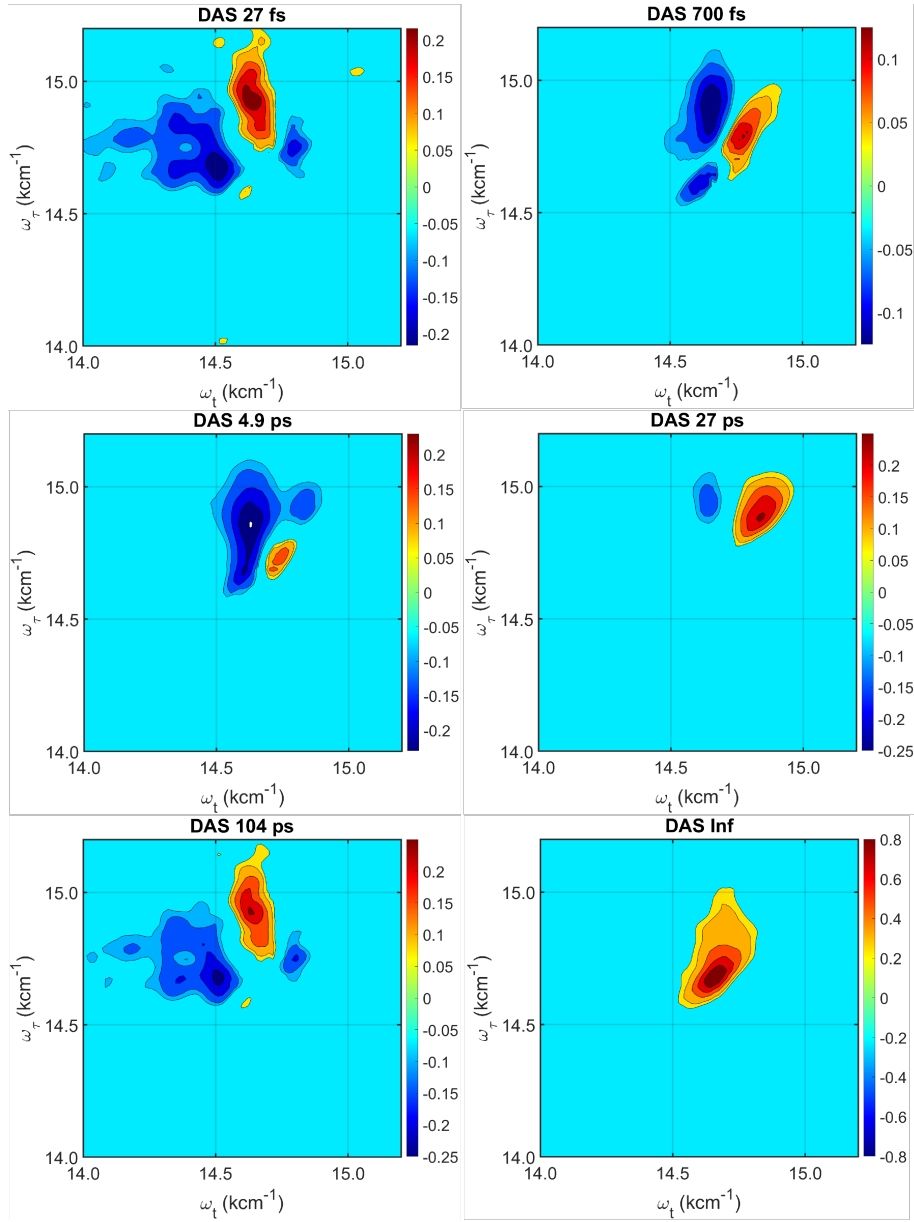


FIG. S2. The 2D DAS with the corresponding resolved decay time constant. The fastest DAS component shows the lifetime of 27 fs. The other components belong to the timescale of 700 fs, 4.9 ps, 27 ps, 104 ps and infinity, respectively.

To find the oscillation frequencies in the residuals, we Fourier transform them and plot the results in Fig. 3(b), (d) and (f) in the main text. For the first trace of the cross peak “X”, we obtain three peaks at the frequencies of 122, 250 and 345 cm^{-1} . Importantly, the resolved vibrations at 250 and 345 cm^{-1} agree with the measurements of other research groups (Ref. 29, 30, 36). From this, we start the fitting procedure by an initial guess of the frequencies at 122, 250 and 345 cm^{-1} . We restrict the mode frequencies in a range of 5 cm^{-1} and fix the initial guess of the lifetime identically to 500 fs, with a range from 0 to ∞ . With these parameters, we obtain a high quality fit with an R-square ≥ 0.95 from the curve fitting toolbox. The trace and the resulting fits are shown as blue square dots and red solid lines in Fig. 4 in the main text, with a confidence range of 95% (green shadow). To achieve a good fit, the first time point has been excluded in the fitting procedure. By these processes, we are able to separate the electronic coherence from ground-state vibrations. The frequency components and the associated decay time constants are shown in Fig. 4 in the main text. We find the frequency of the electronic coherence to be 122 cm^{-1} , with a decay time constant of 180 fs. Clearly, the electronic coherence lasts for two oscillation periods and completely disappears after 600 fs. In addition, the vibrational coherences show the frequencies of 250 and 345 cm^{-1} . The long-lived vibrational coherences

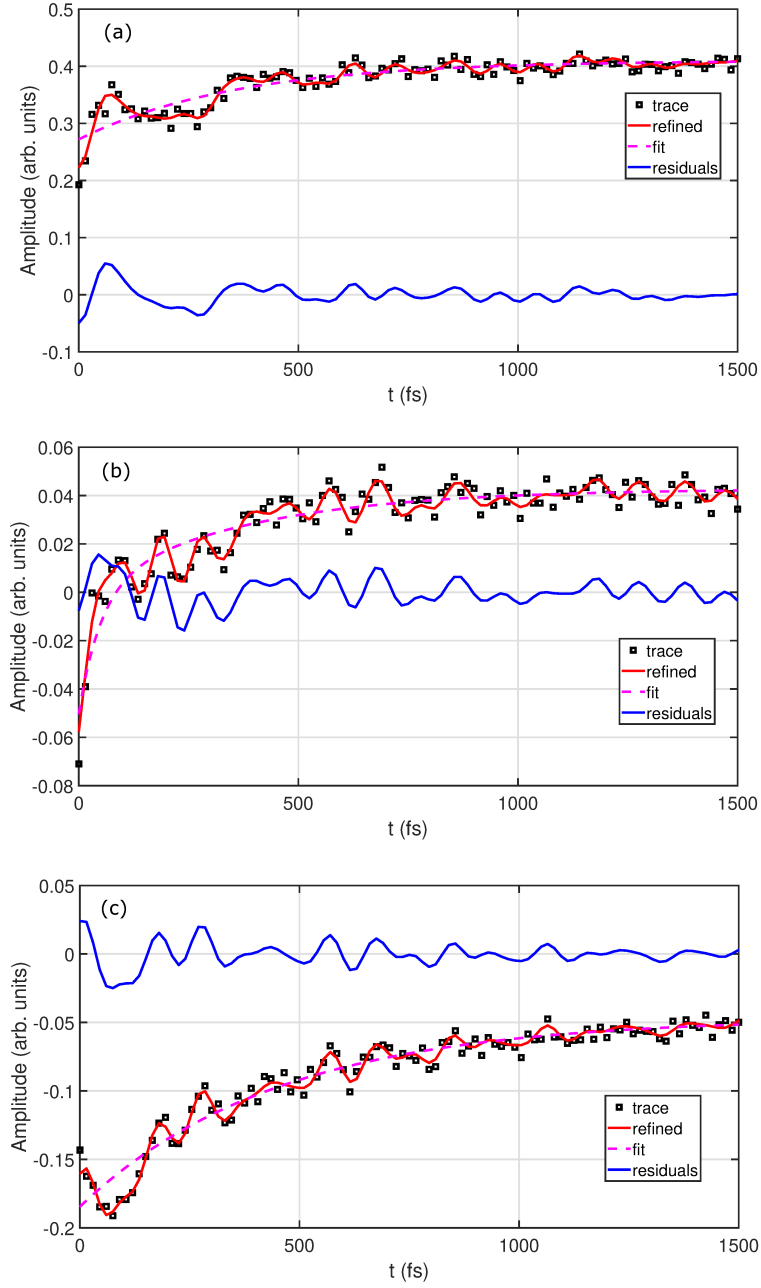


FIG. S3. Raw data of the peaks “X”, “Y” and “Z” are plotted as black dots in (a) to (c). The coordinates of the cross peaks “X”, “Y” and “Z” are $(\omega_\tau, \omega_t) = (14812, 14690)$, $(14690, 14350)$ and $(14874, 14526)$ cm^{-1} , respectively. The treatments of the Tukey window Fourier transforms are shown as red solid lines and the resulting residuals are presented as blue solid lines in (a), (b) and (c), respectively.

decay with time constants of 527 fs and 829 fs in the 2D spectra.

We repeat the same procedure for the traces in Fig. S3(b) and (c) and we plot the filtered data as red solid lines. The exponential fits are performed to obtain the residuals, which are plotted as blue solid lines. The residuals of the cross peak “Y” is uploaded to curve fitting toolbox. The initial, guessed parameters of the vibrations come from the resolved modes in Fig. 3(d) in the main text. They are 64, 262, 336 and 421 cm^{-1} . Based on this, we put the initial values of the vibrational modes into the toolbox and set a range of ± 5 cm^{-1} for the modes. As described before, the initial guess of the timescale is 500 fs for all the modes, with a range from 0 to infinity. The fitting procedure is finished with R-square ≥ 0.95 . The obtained results are shown in the Fig. 4(b) in the main text. All the oscillation frequencies and the associated lifetimes are resolved by this approach. In addition, we repeat the same procedure for

the residuals of Fig. S3(c). The Fourier transform shows the resolved modes with the frequencies 112, 248 and 356 cm^{-1} , which are presented in Fig. 3(f) in the main text. The fitting results are shown in Fig. 4(c) in the main text.

V. 2D POWER SPECTRA OF RESOLVED VIBRATIONS

In the previous section, we have treated the time-resolved traces of the cross peaks in the 2D electronic spectra of the PSII reaction center. However, a global data analysis needs to be performed to resolve the coherent dynamics in all the 2D maps. For this, we process the data of the time series of the 2D electronic spectra. Based on the global fitting approach, we resolve the kinetics of each pixel in the 2D electronic spectra and we remove the kinetics by subtracting the components of exponential fits. We then perform the Fourier transform of the 2D residuals along the waiting time T to obtain the coherent dynamics along the new frequency ω_T . We show the resulting data in Fig. S4 with the corresponding resolved frequencies. In order to identify the origin of these modes, the contours of the 2D spectrum ($T = 435$ fs) are plotted as well and overlap with the 2D power spectra.

VI. 2D CORRELATION ANALYSIS

To verify the origin of the oscillations observed in the 2D electronic spectra, we have performed a cross-correlation analysis of the residuals across $\omega_\tau = \omega_t$. The residual $R(\omega_t, \omega_\tau, T)$ is obtained by subtracting the globally fitted kinetics from the real part of the total 2D electronic spectra. Then, we calculate the correlation coefficients C between two residuals of a pair of conjugated spectral positions in the delay time window up to 2 ps. The delay time steps are equally distributed with intervals of 15 fs. The correlation coefficients are defined as

$$C(\omega_t, \omega_\tau) = \text{corr}[R(\omega_t, \omega_\tau, T), R(\omega_\tau, \omega_t, T)], \quad (\text{S4})$$

where the correlation is evaluated with the respect to T .

In Fig. S5, we depict the 2D correlation map of the residuals obtained after the global fitting of the time sequence of the 2D spectra. It shows a negative magnitude in the upper-left and lower-right parts of the 2D spectrum. Based on Ref. 37, the positive correlation indicates the electronic coherence, while the negative anti-correlation manifests the vibrational coherence. Thus, the strong negative peaks at the center wavelength of the 2D spectra clearly manifest the vibrational origin of the coherent dynamics. In the other words, due to the relatively strong Huang-Rhys factors, the more than 48 resolved vibrational modes (Ref. 36) strongly overlap with the electronic quantum coherence, which challenges the identification of the pure electronic coherence.

VII. MODEL HAMILTONIAN AND REFINED PARAMETERS

In this section, we discuss the model Hamiltonian and its parameters. The detailed information of the tight-binding model and the system-bath interaction model are described in the section of the theoretical calculations in the main text. The PSII reaction center model includes 8 pigments and 4 charge-transfer states, in total 12 singly excited states. We also include 52 double excited states and one additional electronic ground state. Thus, the exciton model involves 65 states. The off-diagonal elements in the Hamiltonian matrix are, in a first step, directly taken from Ref. 9 and used without further changes. The initial, guessed values of the site energies of the 8 pigments are taken from Ref. 9. Then, the population dynamics of the density matrix and the absorption spectra of the PSII reaction center are calculated using the modified Redfield quantum master equation. The obtained results are shown in Fig. S10 for different temperatures. The experimental counterparts are plotted as black square dots. Based on this, we obtain a set of parameters of the site energies and the refined parameters of the bath spectral density. Furthermore, we also optimize the system-bath interaction and the static disorder of each pigment by comparing the bandwidth of the anti-diagonal profile of the 2D electronic spectrum at the initial waiting time. By this, the refined site energies, the parameters of the spectral density and the static disorder (inhomogeneity) are further optimized to the final version used in all the calculations of this work. We give the final form of the Hamiltonian matrix as shown in Tab. S1. All entries are given in units of cm^{-1} .

The parameters of the spectral density are $\eta = 0.68$ and $\omega_c = 350 \text{ cm}^{-1}$, which corresponds to the reorganization energy of 238 cm^{-1} . The static disorder of the chlorophylls are 50 cm^{-1} and of the pheophytins 70 cm^{-1} . Due to the strong electronic interaction due to the static dipole moment of the charge-transfer states, we assume a pretty large value of the static disorder, i.e., $\delta = 100, 200, 200$ and 300 cm^{-1} for the four CT states. The order of the states follows the sites in the system Hamiltonian.

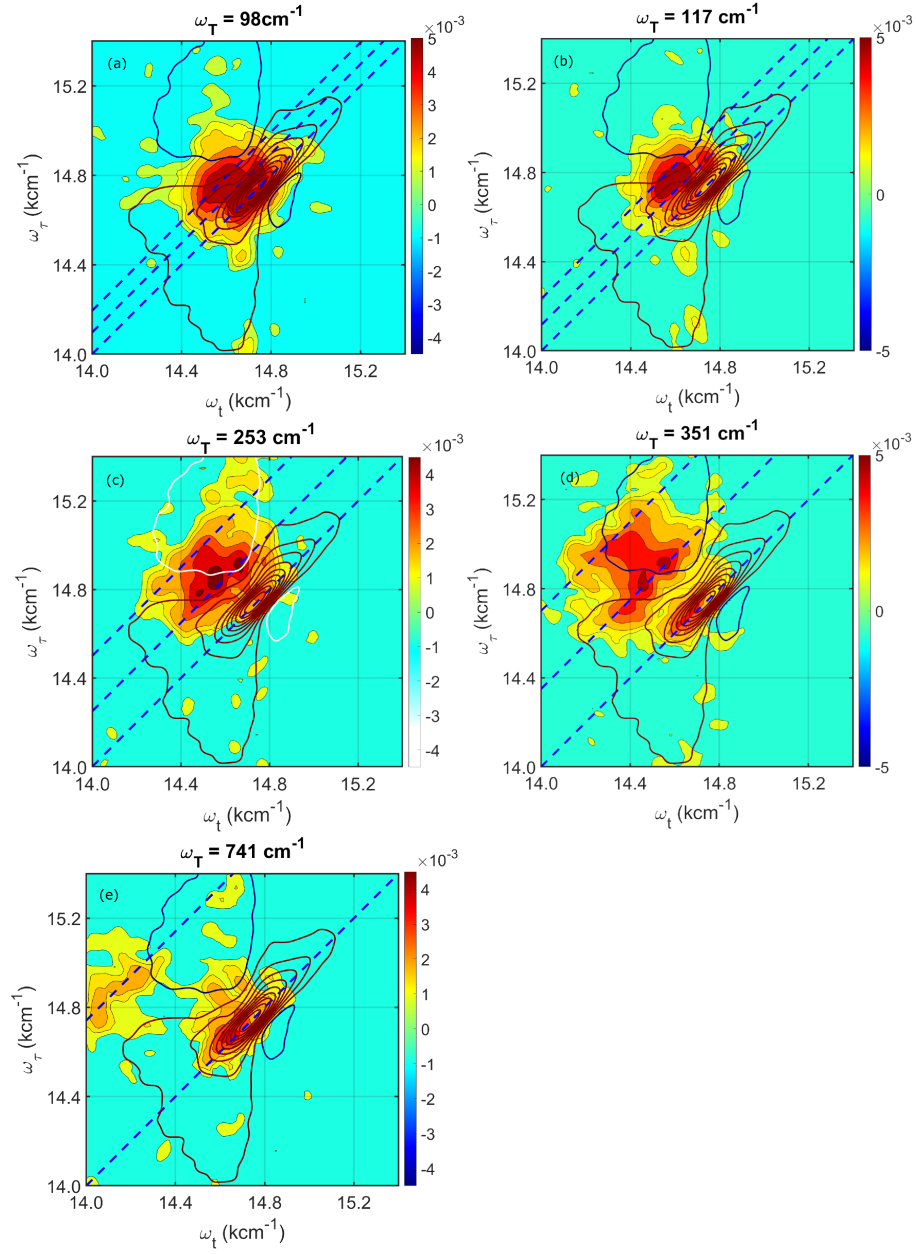


FIG. S4. 2D power spectra of the PSII reaction center, obtained after Fourier transforming the 3D residuals along the waiting time T . Five modes are resolved with the frequencies of 98, 117, 253, 351 and 741 cm^{-1} , respectively. The rephasing part (real) of the 2D electronic spectrum ($T = 435$ fs) is shown as contour lines to locate the origin of the vibrations. In addition, the diagonal lines and the shifted lines according to the resolved frequencies are presented as blue dashed lines in panels (a) to (e).

VIII. THE CALCULATED ABSORPTION SPECTRA AND EXPERIMENTAL RESULTS

In this section, we show the calculated absorption spectra of the reaction center at 6, 77 and 300 K. The corresponding formula used is given in the Eq. (S25) below and the resulting data are shown in Fig. S6. They show an excellent agreement between experimental and theoretical results.

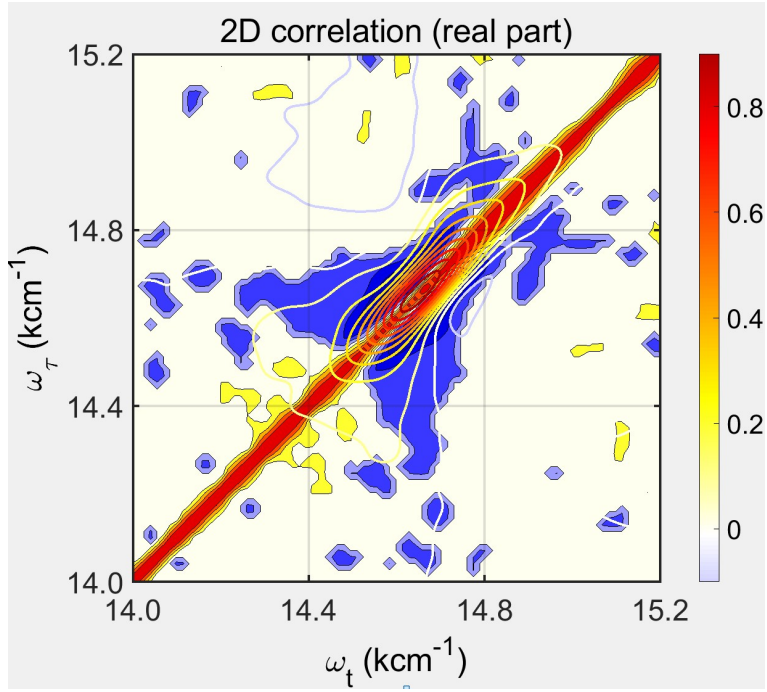


FIG. S5. 2D correlation analysis of the rephasing part (real) of the 2D electronic spectra of the PSII reaction center. The positive magnitude in the spectrum shows a correlation, while the negative magnitude indicates an anti-correlation. The 2D electronic spectrum at $T = 435$ fs is shown as contour lines in order to present the coordinates of the correlations.

TABLE S1. Matrix elements of the single exciton Hamiltonian in basis states. All entries are given in units of cm^{-1} .

	P_{D1}	P_{D2}	Chl_{D1}	Chl_{D2}	Pheo_{D1}	Pheo_{D2}	Chlz_{D1}	Chlz_{D2}	$P_{D2}^+ P_{D1}^-$	$\text{Chl}_{D1}^+ \text{Pheo}_{D1}^-$	$P_{D1}^+ \text{Chl}_{D1}^-$	$P_{D1}^+ \text{Pheo}_{D1}^-$
P_{D1}	14960	150	-42	-55	-6	17	1	1	45	0	0	0
P_{D2}	150	14890	-56	-36	20	-2	1	1	45	0	0	0
Chl_{D1}	-42	-56	14700	7	46	-4	3	0	0	70	0	0
Chl_{D2}	-55	-36	7	14850	-5	37	0	2	0	0	0	0
Pheo_{D1}	-6	20	46	-5	14800	-3	-4	0	0	70	0	0
Pheo_{D2}	17	-2	-4	37	-3	14720	0	-4	0	0	0	0
Chlz_{D1}	1	1	3	0	-4	0	15000	0	0	0	0	0
Chlz_{D2}	1	1	0	2	0	-4	0	14930	0	0	0	0
$P_{D2}^+ P_{D1}^-$	45	45	0	0	0	0	0	0	14882	0	70	0
$\text{Chl}_{D1}^+ \text{Pheo}_{D1}^-$	0	0	70	0	70	0	0	0	0	15692	0	40
$P_{D1}^+ \text{Chl}_{D1}^-$	0	0	0	0	0	0	0	0	70	0	15542	40
$P_{D1}^+ \text{Pheo}_{D1}^-$	0	0	0	0	0	0	0	0	0	40	40	15832

IX. TRANSFORMATION BETWEEN SITE AND EXCITON BASIS

The optimal parameters of the Hamiltonian and the reorganization energies of each site are obtained from the spectroscopic calculations. With those, we can perform the transformation between the site and exciton bases. The transformation matrix is shown in Tab. S2.

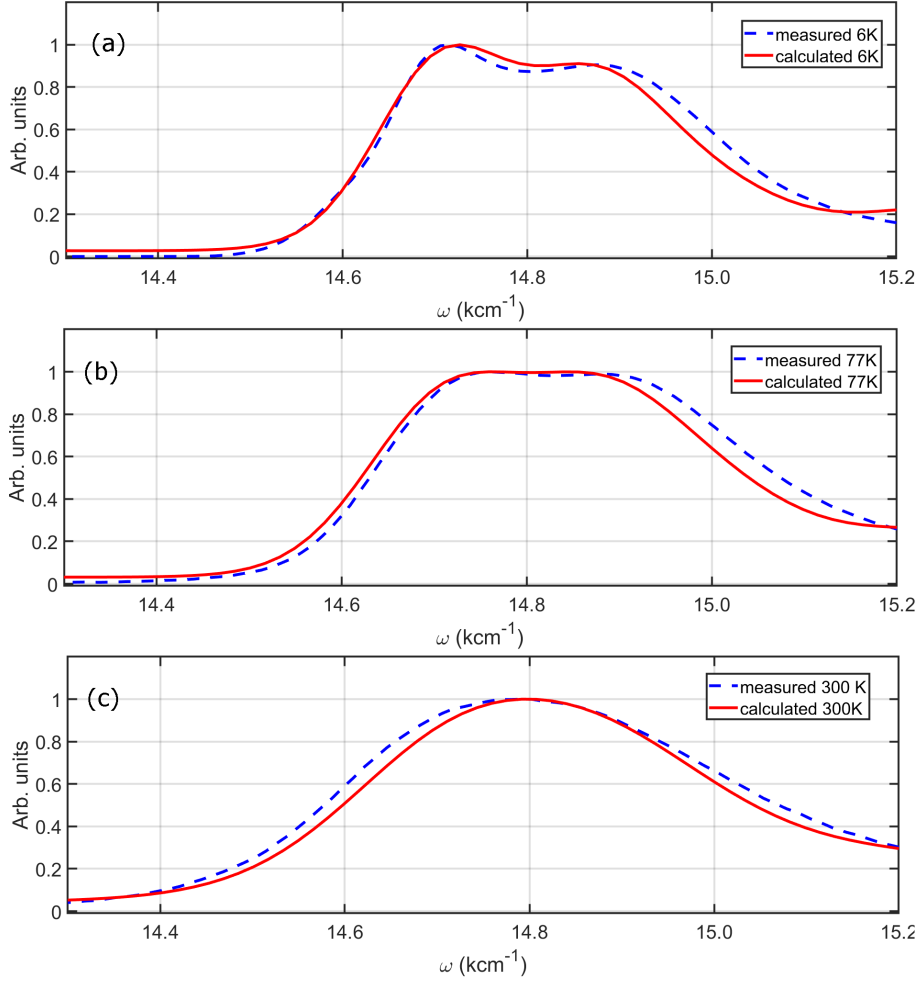


FIG. S6. Experimental (dashed blue lines) and simulated (red solid lines) absorption spectra of the PSII reaction center at 6K (a), 77K (b) and 300 K (c).

X. CALCULATION OF THE 2D ELECTRONIC SPECTRA OF THE PSII REACTION CENTER

In this section, we describe the details of the theoretical calculations of the 2D electronic spectra of the PSII reaction center. The third-order polarization function which defines the 2D spectra is given by

$$P^{(3)}(t) = \int_0^\infty dt_3 \int_0^\infty dt_2 \int_0^\infty dt_1 \hat{R}(t_3, t_2, t_1) E_3(t - t_3) E_2(t - t_3 - t_2) E_1(t - t_3 - t_2 - t_1), \quad (\text{S5})$$

where the response function $\hat{R}(t_3, t_2, t_1)$ is a function of the three times t_1 , t_2 and t_3 . It can be separated into the summation of three parts based on the doorway-window functions (Ref. 41), which has the form

$$\hat{R}(t_3, t_2, t_1) = R^{(c)}(t_3, t_2, t_1) + \sum_{\mu, \nu} \int_0^{t_2} dt'' \int_0^{t''} dt' \bar{W}_\nu(t_3, t_2 - t'') \bar{G}_{\mu\nu}(t'' - t') \bar{D}_\nu(t', t_1) + W_0(t_3) D_0(t_1). \quad (\text{S6})$$

The doorway function \bar{D}_ν represents the population of the ν th exciton created after two interactions with the radiation field. $\bar{G}_{\mu\nu}(t'' - t')$ is the conditional probability for the ν th exciton to hop to the μ th exciton state during $t'' - t'$. \bar{W}_μ is the window function representing the contribution of the μ th exciton to the signal. In the Markov limit, the equation can be simplified to the form

$$\hat{R}(t_3, t_2, t_1) = R^{(c)}(t_3, t_2, t_1) + \sum_{\mu, \nu} W_\nu(t_3) G_{\mu\nu}(t_2) D_\nu(t_1) + W_0(t_3) D_0(t_1), \quad (\text{S7})$$

TABLE S2. Square of the eigenvector elements of the exciton Hamiltonian in the exciton basis with the corresponding site index.

	Chl 1	Chl 2	Chl 3	Chl 4	Pheo 5	Pheo 6	Chl 7	Chl 8	CT 1	CT 2	CT 3	CT 4
Exciton 1	0.0	0.0	0.0	0.00032	0.0	0.00026	0.0	0.99941	0.0	0.0	0.0	0.0
Exciton 2	0.02732	0.00348	0.017	0.0774	0.00694	0.86135	0.0	0.00038	0.00428	0.00138	0.00038	0.0
Exciton 3	0.00705	0.06694	0.55098	0.00219	0.24134	0.01652	0.00019	0.0	0.03325	0.0766	0.00409	0.00085
Exciton 4	0.3944	0.4944	0.0607	0.00014	0.0	0.03906	0.0	0.0	0.00048	0.1069	0.0	0.0
Exciton 5	0.00805	0.05411	0.02225	0.62258	0.2	0.0534	0.0	0.0	0.00449	0.03365	0.0	0.0
Exciton 6	0.00759	0.00071	0.1167	0.24	0.5126	0.02856	0.0	0.0	0.0	0.09296	0.0	0.00036
Exciton 7	0.00582	0.0223	0.01569	0.0017	0.00737	0.0006	0.0	0.0	0.795	0.00835	0.1425	0.0
Exciton 8	0.0	0.0	0.0	0.0	0.0	0.0	0.99951	0.0	0.0	0.0	0.0	0.0
Exciton 9	0.0	0.00278	0.1892	0.0	0.03022	0.0	0.0	0.0	0.0	0.7638	0.00215	0.01069
Exciton 10	0.5482	0.3542	0.02668	0.05542	0.0	0.0	0.0	0.0	0.0147	0.0	0.0	0.0
Exciton 11	0.0007	0.00106	0.00051	0.0	0.0	0.0	0.0	0.0	0.14692	0.00214	0.82555	0.02306
Exciton 12	0.0	0.0	0.0	0.0	0.0001	0.0	0.0	0.0	0.0	0.0	0.025	0.96406

and the time propagation of the conditional probability can be obtained from the equation

$$\frac{d}{dt}G_{\mu\nu}(t) = \sum_{\alpha, \alpha \neq \mu} [K_{\mu\alpha}G_{\alpha\nu}(t) - K_{\alpha\mu}G_{\mu\nu}(t)]. \quad (\text{S8})$$

Here, $K_{\mu\nu} = \int_0^\infty dt \bar{K}_{\mu\nu}(t)$ and $\bar{K}_{\mu\nu}(t) = K_{\mu\nu}^L(t) + K_{\mu\nu}^L(-t)$. The kernel function can be calculated according to the formula

$$K_{\mu\nu}^L(\tau) = K_{\mu\nu}^F(\tau) \{ \dot{g}_{\mu\nu, \nu\mu}(\tau) - [\dot{g}_{\nu\mu, \mu\mu}(\tau) + 2i\lambda_{\nu\mu, \nu\nu}] [\dot{g}_{\nu\nu, \mu\nu}(\tau) - \dot{g}_{\mu\mu, \mu\nu}(\tau) + 2i\lambda_{\mu\nu, \nu\nu}] \}, \quad (\text{S9})$$

for $\tau > 0$. The dots stand for the time derivative, and

$$K_{\mu\nu}^F(\tau) = \exp[-i(\epsilon_\mu - \epsilon_\nu)\tau - g_{\mu\mu, \mu\mu}(\tau) - g_{\nu\nu, \nu\nu}(\tau) + g_{\nu\nu, \mu\mu}(\tau) + g_{\mu\mu, \nu\nu}(\tau) - 2i(\lambda_{\nu\nu, \nu\nu} - \lambda_{\mu\mu, \nu\nu})\tau]. \quad (\text{S10})$$

The $g_{\mu\nu, \mu'\nu'}$ denotes the lineshape function (see Eq. (S24)) and $\lambda_{\mu\nu\mu'\nu'} = -\text{Im} \lim_{\tau \rightarrow \infty} \dot{g}_{\mu\nu, \mu'\nu'}(\tau)$. The coherent part of the response function is written as

$$R^{(c)}(t_3, t_2, t_1) = R(t_3, t_2, t_1) - \sum_{\mu} W_{\mu}(t_3)D_{\mu}(t_1) - W_0(t_3)D_0(t_1), \quad (\text{S11})$$

where three terms contribute to $R(t_3, t_2, t_1)$ according to

$$R(t_3, t_2, t_1) = R_I(t_3, t_2, t_1) + R_{II}(t_3, t_2, t_1) + R_{III}(t_3, t_2, t_1),$$

$$R_I(t_3, t_2, t_1) = -i \sum_{\mu\nu} d_{\mu}d_{\mu}d_{\nu}d_{\nu} \exp[-f_{\mu\nu}^{(1)}(0, t_2 + t_1, t_3 + t_2 + t_1, t_1)] \exp[-i\epsilon_{\mu}(t_3 + t_2) + i\epsilon_{\nu}(t_2 + t_1)],$$

$$R_{II}(t_3, t_2, t_1) = -i \sum_{\mu\nu} d_{\mu}d_{\mu}d_{\nu}d_{\nu} \exp[-f_{\mu\nu}^{(1)}(0, t_1, t_3 + t_2 + t_1, t_2 + t_1)] \exp[-i\epsilon_{\mu}t_3 + i\epsilon_{\nu}t_1],$$

$$R_{III}(t_3, t_2, t_1) = -i \left\{ \sum_{\mu\nu\alpha} d_{\mu\bar{\alpha}}d_{\nu\bar{\alpha}}d_{\nu}d_{\mu} \exp[-f_{\mu\nu, \bar{\alpha}}^{(2)}(t_1, t_2 + t_1, t_3 + t_2 + t_1, 0)] \exp[-i\epsilon_{\mu}(t_3 + t_2 + t_1) + i\epsilon_{\nu}t_3 + i\epsilon_{\nu}t_2] \right\}^*. \quad (\text{S12})$$

Here, $f^{(1)}$ and $f^{(2)}$ are given by

$$\begin{aligned} f_{\mu\nu}^{(1)}(\tau_1, \tau_2, \tau_3, \tau_4) &= g_{\mu\mu}(\tau_3 - \tau_4) - g_{\mu\nu}(\tau_2 - \tau_4) + g_{\mu\nu}(\tau_1 - \tau_4) \\ &\quad + g_{\mu\nu}(\tau_2 - \tau_3) - g_{\mu\nu}(\tau_1 - \tau_2) + g_{\nu\nu}(\tau_1 - \tau_2), \\ f_{\mu\nu, \bar{\alpha}}^{(2)}(\tau_1, \tau_2, \tau_3, \tau_4) &= g_{\mu\mu}(\tau_3 - \tau_4) - g_{\mu\bar{\alpha}}(\tau_3 - \tau_4) + g_{\mu\bar{\alpha}}(\tau_2 - \tau_4) + g_{\mu\nu}(\tau_2 - \tau_4) \\ &\quad + g_{\mu\nu}(\tau_1 - \tau_4) - g_{\mu\bar{\alpha}}(\tau_2 - \tau_3) + g_{\mu\nu}(\tau_2 - \tau_3) - g_{\mu\nu}(\tau_1 - \tau_3) \\ &\quad + g_{\bar{\alpha}\bar{\alpha}}(\tau_2 - \tau_3) - g_{\bar{\alpha}\nu}(\tau_2 - \tau_3) + g_{\bar{\alpha}\nu}(\tau_1 - \tau_3) - g_{\bar{\alpha}\nu}(\tau_1 - \tau_2) + g_{\nu\nu}(\tau_1 - \tau_2). \end{aligned} \quad (\text{S13})$$

The remaining terms are given by

$$\sum_{\mu} W_{\mu}(t_3)D_{\mu}(t_1) = -i \sum_{\mu} d_{\mu}^2 \exp[i\epsilon_{\mu}t_1 - g_{\mu\mu}^*(t_1)] \{d_{\mu}^2 \exp[-i\epsilon_{\mu}t_3 - g_{\mu\mu}^*(t_3) + 2i\lambda_{\mu\mu}t_3] - \sum_{\nu} d_{\mu,\bar{\nu}}^2 - \sum_{\nu} d_{\mu,\bar{\nu}}^2\} \times \exp[-i(\epsilon_{\text{bar}\nu} - \epsilon_{\mu})t_3 - g_{\mu\mu}(t_3) - g_{\bar{\nu}\bar{\nu}}(t_3) + 2g_{\mu\bar{\nu}}(t_3) + 2i(\lambda_{\mu\bar{\nu}} - \lambda_{\mu\mu})t_3], \quad (\text{S14})$$

and

$$W_0(t_3)D_0(t_1) = -i \sum_{\mu\nu} d_{\nu}^2 d_{\mu}^2 \exp[i\epsilon_{\nu}t_1 - g_{\nu\nu}^*(t_1)] \times \exp[-i\epsilon_{\mu}t_3 - g_{\mu\mu}(t_3)], \quad (\text{S15})$$

$$\sum_{\mu\nu} W_{\mu}(t_3)G_{\mu\nu}(t_2)D_{\nu}(t_1) = -i \sum_{\mu\nu} d_{\nu}^2 \exp[i\epsilon_{\nu}t_1 - g_{\nu\nu}^*(t_1)]G_{\mu\nu}(t_2) \times \{d_{\mu}^2 \exp[-i\epsilon_{\mu}t_3 - g_{\mu\mu}^*(t_3) + 2i\lambda_{\mu\mu}t_3] - \sum_{\mu} d_{\mu,\bar{\nu}}^2 \exp[-i(\epsilon_{\mu})t_3 - g_{\mu\mu}(t_3) - g_{\bar{\nu}\bar{\nu}}(t_3) + 2g_{\mu\bar{\nu}} + 2i(\lambda_{\mu\bar{\nu}} - \lambda_{\mu\mu})t_3]\}. \quad (\text{S16})$$

XI. ANTI-DIAGONAL BANDWIDTH IN THEORY AND EXPERIMENT

In this section, we show the anti-diagonal profile of the calculated 2D spectra and compare it to the experimental counterpart. We show the results in Fig. S7. The anti-diagonal profile of the calculated 2D spectrum at $T = 30$ fs (real rephasing part) is plotted as blue solid line. The experimental counterpart is shown as black square dots. Both agree well quantitatively, which demonstrates the validity of our model and parameters to capture the main dephasing features in our spectroscopic calculations.

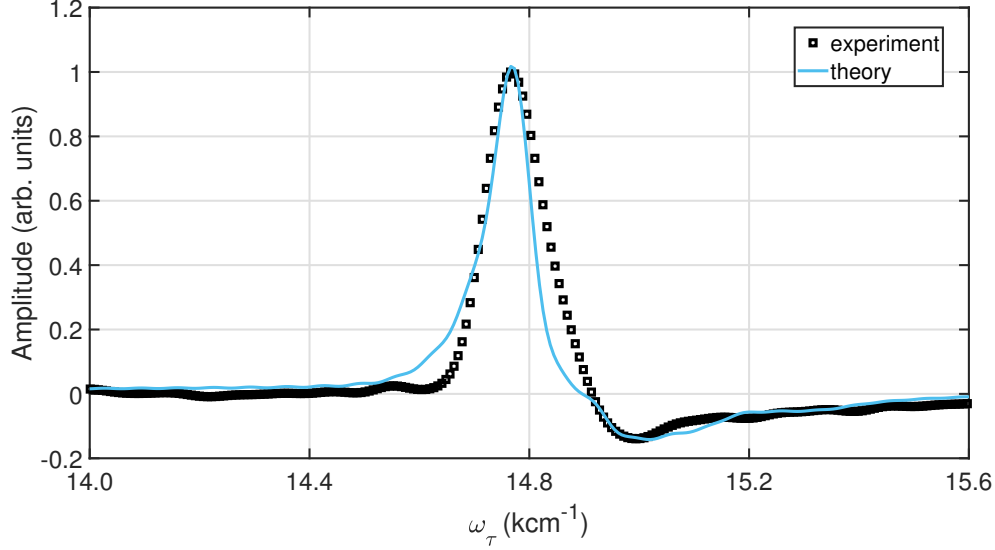


FIG. S7. Anti-diagonal profile of the calculated 2D spectrum (real rephasing part, blue solid line) and the experimental counterpart (black square dots). The selected waiting time is $T = 30$ fs at the temperature of 20 K.

XII. MEASURING OF 2D SPECTRA WITH DIFFERENT COHERENCE TIMES

In this section, we address the question of length of the coherence time τ window in our measurement. For this, we plot one of our 2D spectroscopic measurements at $T = 30$ fs. We show the measured results in Fig. S8. We depict the results with different colors, as indicated in the colorbar, to demonstrate the results after -400 fs is very weak and, thus, is expected to hardly contribute to the signal in the measurement. Hence, the τ scanning window from -450 fs to 250 fs is long enough for the detections carried out in this work. In addition, we also plot the detected profiles of spectra at different τ times. In Fig. S9, we show the photo-echo signals for different times from 0 to -350 fs.

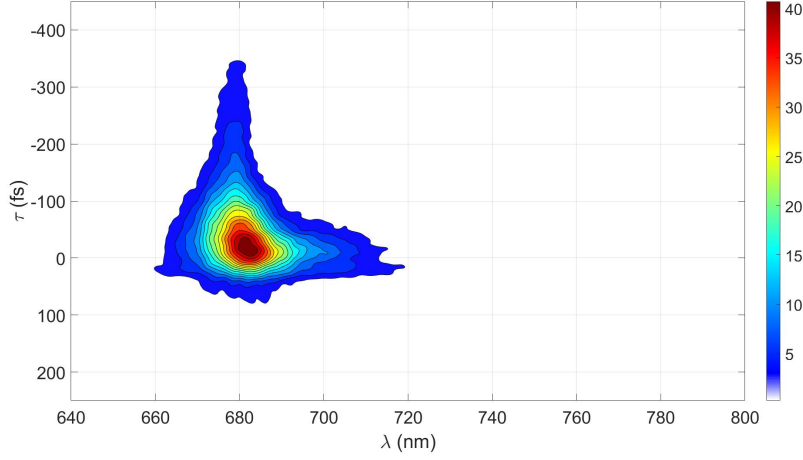


FIG. S8. The measured signal of photo-echo in the coherence time window between -450 fs to 250 fs.

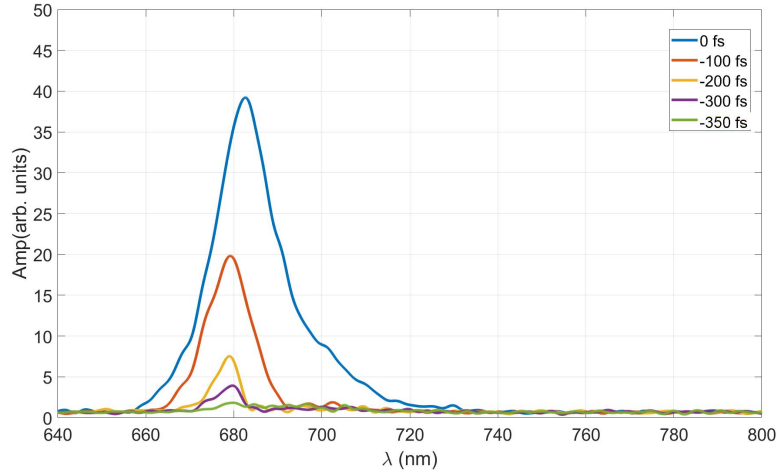


FIG. S9. Time-dependent measured spectral profiles for the selected coherence times of $\tau = 0$ to -350 fs.

XIII. MODIFIED REDFIELD QUANTUM MASTER EQUATION

The modified Redfield theory can be derived from the Nakajima-Zwanzig equation using a scheme for the separation of the total Hamiltonian which does not treat the whole system-bath interaction term H_{SB} perturbatively Ref. 56 and 57. Instead, the Hamiltonian is separated as

$$\begin{aligned}
 H_0 &= H_S + H_B + \sum_{\mu} |\mu\rangle \langle \mu| H_{SB} |\mu\rangle \langle \mu|, \\
 H' &= \sum_{\mu\nu, \mu \neq \nu} |\mu\rangle \langle \mu| H_{SB} |\nu\rangle \langle \nu|,
 \end{aligned}
 \tag{S17}$$

where $|\mu\rangle$ are eigenstates of H_S and H' collects the off-diagonal terms of the system-bath interaction in the exciton basis. In this basis, H_0 is diagonal and the matrix elements read

$$\langle \mu| H_0 |\mu\rangle = \epsilon_{\mu} - \lambda_{\mu\mu\mu\mu} + H_B(\mu),
 \tag{S18}$$

where ϵ_μ is the exciton energy of the system Hamiltonian and

$$\lambda_{\mu\nu\mu'\nu'} = \sum_m \langle \mu | K_m | \nu \rangle \langle \mu' | K_m | \nu' \rangle \sum_j \frac{c_{mj}^2}{2m_{mj}\omega_{mj}^2} \quad (\text{S19})$$

is the weighted reorganization energy. Moreover,

$$H_B(\mu) = \frac{1}{2} \sum_\xi \left(\frac{p_\xi^2}{m_\xi} + m_\xi \omega_\xi^2 \left(x_\xi + \sum_k \frac{\langle \mu | K_k | \mu \rangle}{m_\xi \omega_\xi^2} \right)^2 \right) \quad (\text{S20})$$

describes a bath of harmonic oscillators with mass m_ξ , frequency ω_ξ and momentum p_ξ , shifted according to the coupling with the exciton state $|\mu\rangle$.

In addition to the redefinition of the system part and the bath Hamiltonian, one has to define a different type of projection operator which only projects on the diagonal part of the system density matrix in the eigenstate basis,

$$\tilde{P} = \sum_{\mu=0}^N P_\mu \quad \text{with} \quad P_\mu \cdot = R_{eq}^\mu \text{tr}\{|\mu\rangle \langle \mu| \cdot\}, \quad (\text{S21})$$

where P_μ is the projector onto the μ th excitonic state and $R_{eq}^\mu = \exp(-\beta H_B(\mu))$ is the equilibrium density matrix of the bath when the system is in the excitonic state $|\mu\rangle$.

Inserting these definitions into the Nakajima-Zwanzig equation, determining the H' up to second order and invoking the time-dependent population transfer rate one obtains an equation of motion for the time-dependent populations as

$$\frac{\partial}{\partial t} \rho_{\mu\mu}(t) = \sum_{\nu \neq \mu} (R_{\mu\nu\nu}(t) \rho_{\nu\nu} - R_{\nu\nu\mu}(t) \rho_{\mu\mu}), \quad (\text{S22})$$

where the population transfer rates $R_{\mu\nu\nu}$ (Ref. 41) are given by

$$\begin{aligned} R_{\mu\nu\nu}(t) &= 2 \text{Re} \int_0^t d\tau \text{tr}\{|\nu\rangle \langle \nu| \exp(-iH_0\tau) H' |\mu\rangle \langle \mu| R_{eq}^\mu \exp(iH_0\tau) H'\} \\ &= 2 \text{Re} \int_0^t d\tau \exp(-i\omega_{\mu\nu}\tau - g_{\mu\mu\mu\mu}(\tau) - g_{\nu\nu\nu\nu}(\tau) + g_{\nu\nu\mu\mu}(\tau) + g_{\mu\mu\nu\nu}(\tau) - 2i(\lambda_{\nu\nu\nu\nu} - \lambda_{\mu\mu\nu\nu})\tau) \\ &\quad \times \{\dot{g}_{\mu\nu\nu\mu}(\tau) - [\dot{g}_{\nu\nu\nu\nu}(\tau) - \dot{g}_{\nu\nu\mu\mu}(\tau) + 2i\lambda_{\nu\nu\nu\nu}][\dot{g}_{\nu\nu\mu\nu}(\tau) - \dot{g}_{\mu\mu\nu\nu}(\tau) + 2i\lambda_{\mu\nu\nu\nu}]\}. \end{aligned} \quad (\text{S23})$$

The lineshape function $g_{\mu\nu\mu'\nu'}(t)$ can be written as the two-time integral of the bath correlation function

$$\begin{aligned} g_{\mu\nu\mu'\nu'}(t) &= \sum_k \langle \mu | K_k | \nu \rangle \langle \mu' | K_k | \nu' \rangle \int_0^t d\tau \int_0^\tau d\tau' C(\tau'), \\ \text{with } C(t) &= \int_{-\infty}^{\infty} \frac{d\omega}{\pi} J(\omega) \frac{e^{i\omega t}}{e^{\beta\omega} - 1}. \end{aligned} \quad (\text{S24})$$

In Eq. (S23), we have used the cumulant expansion technique up to second order in the system-bath coupling and took the independent bath model into account. The absorption lineshape within the modified Redfield theory is given by

$$I(\omega) = \text{Re} \sum_\mu d_\mu \int_0^\infty dt \exp[i(\omega - \omega_{\mu 0})t - g_{\mu\mu\mu\mu}(t) - \frac{1}{2} \sum_{\nu \neq \mu} \int_0^t R_{\mu\nu\nu\nu}(\tau)]. \quad (\text{S25})$$

as detailed in Ref. 53.

The well developed modified Redfield theory has been described above. Next, based on the population transfer term, Eq. (S22), we derive the extended quantum master equation, in which the population terms are given as

$$\begin{aligned} \frac{\partial}{\partial t} \rho(t) &= -i[H + F(t), \rho(t)] - \Re\{\rho(t)\}, \\ \Re\{\rho(t)\}_{\mu\mu} &= \sum_{\nu \neq \mu} (R_{\mu\nu\nu\nu}(t) \rho_{\nu\nu} - R_{\nu\nu\mu\mu}(t) \rho_{\mu\mu}). \end{aligned} \quad (\text{S26})$$

Here, $\Re\{\rho(t)\}_{\mu\mu}$ is the diagonal term of the relaxation operator, which was described in Ref. 55 and $F(t)$ is the time-dependent system-field interaction term.

The off-diagonal terms $\Re\{\rho(t)\}_{\mu\nu}$ in the master equation are required to describe decoherence of excited states and electronic dephasing between ground and excited states. Here, we use the relation $1/T_2 = 1/2T_1 + 1/T_2^*$ to estimate the different contributions to the dephasing rate. T_2 is the transverse relaxation time, T_1 , T_2^* are called longitudinal relaxation time and pure dephasing time, respectively (Ref. 56). In detail, $1/T_1 = \sum_{e \neq \mu} R_{\mu\mu ee} + \sum_{e \neq \nu} R_{\nu\nu ee}$ and $1/T_2^*$ is given by the first derivative of the lineshape function $g_{\mu\mu\nu\nu}(t)$. Therefore, the off-diagonal terms of the excited states and between ground and excited states can be written as

$$\begin{aligned}\Re\{\rho(t)\}_{\mu\nu} &= \left\{ \frac{1}{2} \left(\sum_{e \neq \mu} R_{\mu\mu ee}(t) + \sum_{e \neq \nu} R_{\nu\nu ee}(t) \right) + \dot{g}_{\mu\mu\nu\nu}(t) \right\} \rho_{\mu\nu}(t), \\ \Re\{\rho(t)\}_{\mu 0} &= \left\{ \frac{1}{2} \left(\sum_{m \neq \mu} R_{m\mu mm}(t) + \sum_{n \neq m} R_{nn mm}(t) \right) + \dot{g}_{\mu\mu\mu\mu}(t) \right\} \rho_{\mu 0}(t).\end{aligned}\tag{S27}$$

XIV. MODEL OF DIMER SYSTEMS

In the last section, we have constructed a model of the PSII reaction center and optimized the parameters for the spectroscopic calculations. Here, we study the coherent dynamics of the primary charge transfer in the dimer system. For this, we construct a dimer model with a charge-transfer state. In the first case, we examine the coherent dynamics of the pigments of Chl_{D1} and Pheo_{D1} . One additional charge-transfer state $\text{Chl}_{D1}^+ \text{Pheo}_{D1}^-$ is included. The system Hamiltonian is given by

$$H_s = \begin{bmatrix} \epsilon_{\text{Chl}_{D1}} & V & V_{CT} \\ V & \epsilon_{\text{Pheo}_{D1}} & V_{CT} \\ V_{CT} & V_{CT} & \epsilon_{CT} \end{bmatrix},\tag{S28}$$

where the site energies are $\epsilon_{\text{Chl}_{D1}} = 14700 \text{ cm}^{-1}$, $\epsilon_{\text{Pheo}_{D1}} = 14800 \text{ cm}^{-1}$ and $\epsilon_{CT} = 15692 \text{ cm}^{-1}$. Moreover, the excitonic interaction between two pigments is $V = 46 \text{ cm}^{-1}$ and the couplings between exciton and charge-transfer state is $V_{CT} = 70 \text{ cm}^{-1}$. The parameters of the spectral density are $\eta = 0.68$ and $\omega_c = 350 \text{ cm}^{-1}$. To take into account the strong system-bath interaction, we assume the interaction of the charge-transfer state with the environment to be three times stronger than the one of the pigment. For this, we assign the system-bath interaction factor to 3.0 for the charge-transfer state, the others are assumed to be 1.0. All the parameters are taken from the set of optimal parameters based on the 2D spectroscopic calculations of the PSII reaction center. We employ the QUAPI approach to obtain numerically exact results of the dynamics and we plot the time-evolved dynamics in Fig. S10. The calculations are performed at 20 K. At this low temperature, the memory timescale of the system has to be carefully treated. We use the QUAPI parameters $K_{\text{max}} = 9$ and $\Delta t = 30 \text{ fs}$, thus, the total memory time $\tau = 270 \text{ fs}$ to achieve numerical convergence. In Fig. S10, we observe clear evidence of electronic quantum coherence with a period of 273 fs and with a lifetime of 177 fs. Hence, electronic coherence persists for 600 fs at 20 K. More interestingly, the calculated results do not show any evidence of an oscillatory dynamics in the charge-transfer state $\text{Chl}_{D1}^+ \text{Pheo}_{D1}^-$. Our model and calculations manifest that the strong static dipole moment of the charge-transfer state results in a strong interaction with the environment. It significantly reduces the amplitude of the electronic coherence. We may conclude that, even at low temperature of 20 K, there is no substantial role of electronic coherence during the charge-transfer process.

We repeat the same procedure to calculate the population dynamics of the pigments P_{D1} and P_{D2} . The system Hamiltonian of the dimer is taken from the elements of the reaction-center Hamiltonian

$$H_s = \begin{bmatrix} \epsilon_{P_{D1}} & V & V_{CT} \\ V & \epsilon_{P_{D2}} & V_{CT} \\ V_{CT} & V_{CT} & \epsilon_{CT} \end{bmatrix},\tag{S29}$$

where the $V = 150 \text{ cm}^{-1}$ and $V_{CT} = 45 \text{ cm}^{-1}$. The site energies are $\epsilon_{P_{D1}} = 14960 \text{ cm}^{-1}$ and $\epsilon_{P_{D2}} = 14890 \text{ cm}^{-1}$. The site energy of the charge-transfer state is $\epsilon_{CT} = 14882 \text{ cm}^{-1}$. Other parameters are exactly the same as used in the model of the first case. We construct the dimer model and perform the calculations by QUAPI. The time-resolved population dynamics are calculated and shown in Fig. S11. We observe that the electronic coherence between P_{D1} and P_{D2} persists for 400 fs at 20 K, although with the strong excitonic coupling between them ($V = 150 \text{ cm}^{-1}$). Moreover, we do not observe any electronic coherence of the charge-transfer state $P_{D2}^+ P_{D1}^-$.

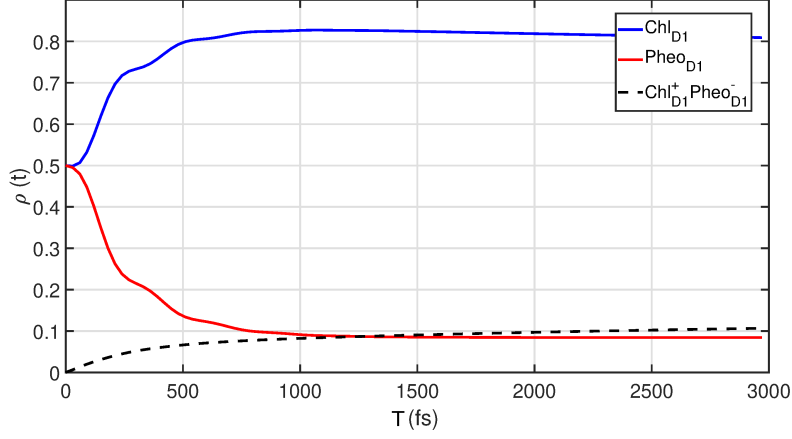


FIG. S10. Population dynamics of the reduced density matrix of the dimer model. The population of Chl_{D1} and Pheo_{D1} are plotted as blue and red solid lines. They show clear evidence of electronic coherence (period of 273 fs) with the lifetime of 177 fs. The results do not show any evidence of oscillations in the charge-transfer state $\text{Chl}_{\text{D1}}^+ \text{Pheo}_{\text{D1}}^-$. The calculations are performed at 20 K.

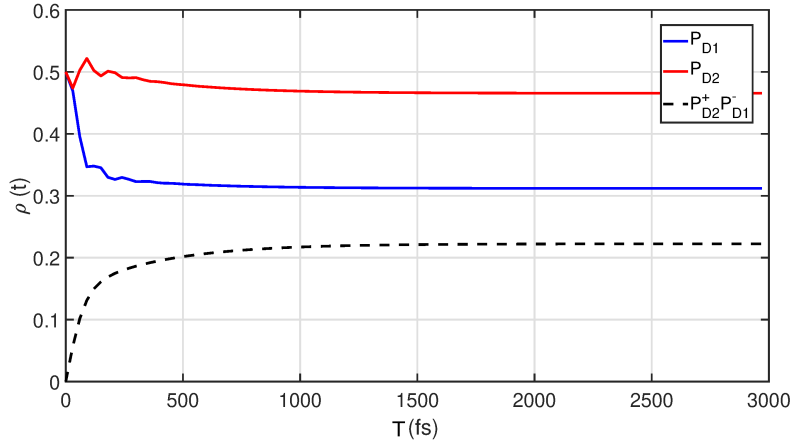


FIG. S11. Population dynamics of P_{D1} , P_{D2} and $P_{\text{D2}}^+ P_{\text{D1}}^-$. The electronic coherence persists for 400 fs. There is no evidence of electronic coherence of the charge-transfer state $P_{\text{D2}}^+ P_{\text{D1}}^-$. The calculations are performed at 20 K.

Moreover, we examine the lifetime of the electronic coherence for varying temperature. We change the temperature to 80 K and calculate the population dynamics of the dimer model. The results are shown in Fig. S12 and S13, respectively. In Fig. S12, the population dynamics of Chl_{D1} and Pheo_{D1} are plotted as blue and red solid lines. The dynamics of the charge-transfer state of $\text{Chl}_{\text{D1}}^+ \text{Pheo}_{\text{D1}}^-$ is plotted as black dashed line. It shows that the electronic coherence between cofactors of Chl_{D1} and Pheo_{D1} vanishes with increasing temperature to 80 K. However, the calculated results in Fig. S13 show the electronic coherence in the radical pairs of P_{D1} and P_{D2} . The data analysis shows that the magnitude and lifetime of the electronic coherence is significantly reduced due to the increased temperature. The results yield the lifetime of electronic coherence of 120 fs at 80 K.

We further increase the temperature to 300 K and present the calculated results in Fig. S14 and Fig. S15, respectively. In Fig. S14, the population dynamics of the cofactors are plotted as blue and red solid lines. The charge-transfer state is depicted as black dashed line. No evidence of electronic coherence during the population transfer between the cofactors and the charge-transfer process is found. Moreover, compared to the case of 80 K, the rate of the energy transfer from the pigments to the charge-transfer state is enhanced when temperature is increased. Interestingly, the calculations of the population dynamics between P_{D1} and P_{D2} in Fig. S15 show rather weak signatures of electronic coherence even at room temperature (300 K). The blue and red solid lines reveal a small magnitude of electronic

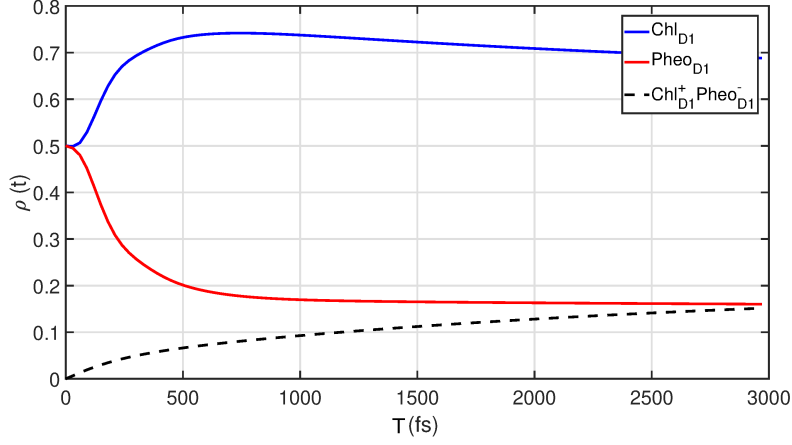


FIG. S12. Population dynamics of the cofactors Chl_{D1} , Pheo_{D1} and the associated charge-transfer state $\text{Chl}_{\text{D1}}^+ \text{Pheo}_{\text{D1}}^-$. The calculations are performed at 80 K.

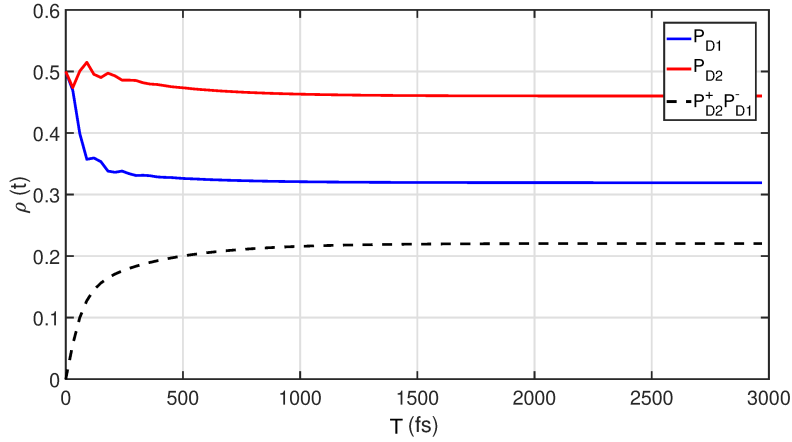


FIG. S13. Population dynamics of P_{D1} , P_{D2} and $\text{P}_{\text{D2}}^+ \text{P}_{\text{D1}}^-$ at 80 K.

quantum coherence at initial time which rapidly disappears within 120 fs. Due to the strong electronic interaction between P_{D1} and P_{D2} , the electronic coherence could survive for more than 100 fs at room temperature. The energy gap of P_{D1} and P_{D2} in the excitonic basis is 340 cm^{-1} , which yields the electronic coherence with a period of 98 fs. Thus, even at room temperature, the electronic quantum coherence between P_{D1} and P_{D2} oscillates for more than one period in the PSII reaction center. However, we do not observe any coherent dynamics of the charge-transfer state $\text{P}_{\text{D2}}^+ \text{P}_{\text{D1}}^-$, which implies that the observed coherence in the cofactors does not participate in the process of charge transfer. Based on the estimate of magnitude of the population of the charge-transfer state, we conclude that the rate of charge transfer is strongly enhanced by increasing of temperature.

In order to examine the role of vibrational coherence, we also study the population dynamics of two dimer systems in the presence of an interaction with an additional vibrational mode. We pick up the vibrational mode of 340 cm^{-1} in the PSII reaction center and assume the Huang-Rhys factor of this particular mode to be $S = 0.01$. We calculate the population dynamics of both systems and show the results in Fig. S16 and S17, respectively. In Fig. S16, the population dynamics of Chl_{D1} and Pheo_{D1} are plotted as blue and red solid lines, respectively. The dynamics of the charge-transfer state is plotted as black dashed line. It shows long-lived electronic coherence between Chl_{D1} and Pheo_{D1} . However, the oscillatory dynamics is absent in the charge-transfer state $\text{Chl}_{\text{D1}}^+ \text{Pheo}_{\text{D1}}^-$. The calculation is performed at 20 K. Interestingly, the calculated results do not show any signature of vibrational coherence. This reveals a weak vibronic interaction ($S = 0.01$). Furthermore, off-resonance of the vibrational mode of 340 cm^{-1} and the excitonic energy gap of Chl_{D1} and Pheo_{D1} significantly reduces the magnitude of vibrational coherence. The

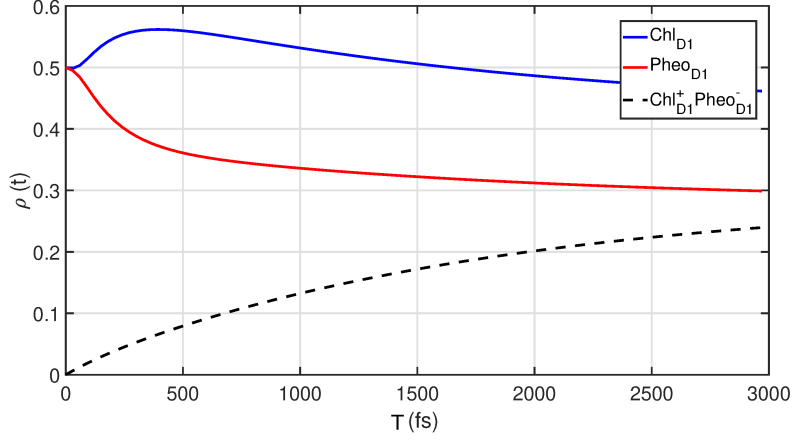


FIG. S14. Population dynamics of Chl_{D1} and Pheo_{D1} at 300 K.

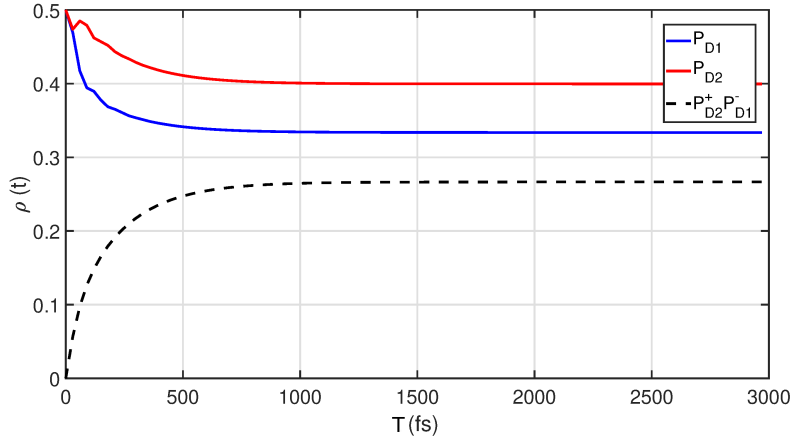


FIG. S15. Time-resolved dynamics of the population transfer between P_{D1} and P_{D2} at 300 K.

calculated population dynamics of P_{D1} and P_{D2} are shown in Fig. S17. The oscillatory dynamics of the red and blue solid lines manifests the mixture of electronic and vibrational coherence when compared to the population in Fig. S11. However, the electronic and vibrational coherence is still absent in the charge-transfer state $P_{D2}^+ P_{D1}^-$ due to the strong system-bath interaction.

To study the role of temperature, we calculate the population dynamics of the dimer model systems for varying temperature. In Fig. S18, we show the population dynamics of Chl_{D1} , Pheo_{D1} and the associated charge-transfer state. With increasing temperature, the electronic coherence is strongly reduced. The calculations of P_{D1} and P_{D2} show a different picture in Fig. S19. Here, the electronic coherence strongly mixes with vibrational coherence at 80 K. However, there is no strong signature of coherence in the charge transfer state $P_{D2}^+ P_{D1}^-$. We further perform the calculation of the population dynamics at 300 K and show them in Fig. S20 and S21, respectively. In Fig. S20, no evidence of electronic coherence between pigments and also the charge-transfer state is revealed. In addition, compared to the dynamics at 80 K, the efficiency of charge transfer is further strongly enhanced by increasing of temperature. More important, it shows only weak evidence of electronic and vibrational coherences in the process of energy transfer of P_{D1} and P_{D2} in Fig. S21.

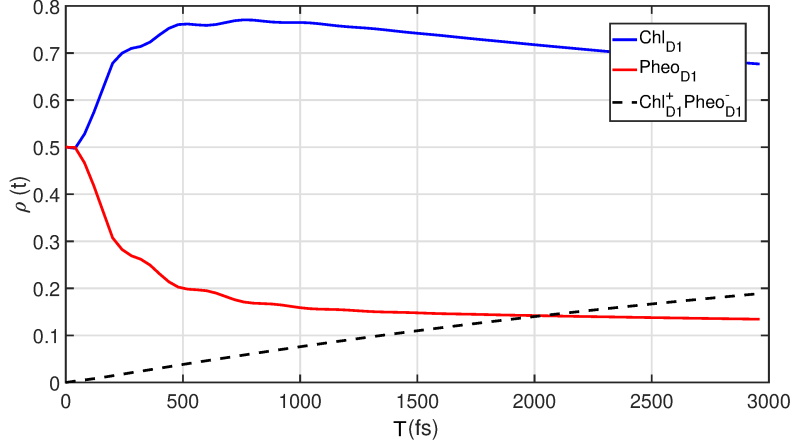


FIG. S16. Population dynamics of cofactors Chl_{D1} and Pheo_{D1} . The spectral density includes an underdamped mode with parameters, $S = 0.01$ and $\omega_{\text{vib}} = 340 \text{ cm}^{-1}$. The calculations are performed at 20 K.

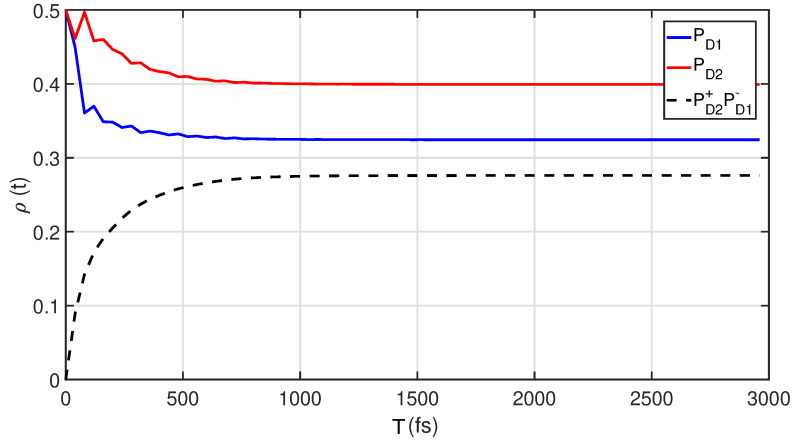


FIG. S17. Population dynamics of cofactors of P_{D1} and P_{D2} at 20 K. An underdamped mode is included in the spectral density for the calculation, $S = 0.01$ and $\omega_{\text{vib}} = 340 \text{ cm}^{-1}$.

XV. THE MODEL OF THE PSII REACTION CENTER

Motivated by the numerical results for the dimer model, we extend our calculations to the PSII reaction center. The system Hamiltonian includes 8 cofactors, which is quite challenging for the numerically exact QUAPI method. Due to the long memory time at low temperature of 20 K, we cannot obtain converged results with the limited number of $K_{\text{max}} = 3$ in QUAPI with present-day hardware capacities. An increasing of K_{max} induces an exponential growth of the memory space in the computer. Thus, we only can carry out calculations of the population dynamics at 80 and 300 K. In addition, we need to turn off the underdamped mode in the spectral density to simplify the calculations, i.e., by setting $S = 0$. Then, the calculated population dynamics only contains electronic coherence by construction. We show the calculated results for 80 K in Fig. S22. The initial relative populations are assumed to be 0.125. The population are propagated to 3000 fs. At 80 K, the weak magnitude of the electronic coherence between P_{D1} and P_{D2} persists for 250 fs at 80 K.

Moreover, we change temperature to 300 K and keep the remaining parameters unchanged. We obtain the calculated population dynamics of the PSII reaction center and show them in Fig. S23. They show a quite weak magnitude of coherence between P_{D1} and P_{D2} at initial population time, which is due to the strong excitonic interaction between them, $V = 150 \text{ cm}^{-1}$. There is no evidence of electronic coherence in the other electronic or charge-transfer states at room temperature.

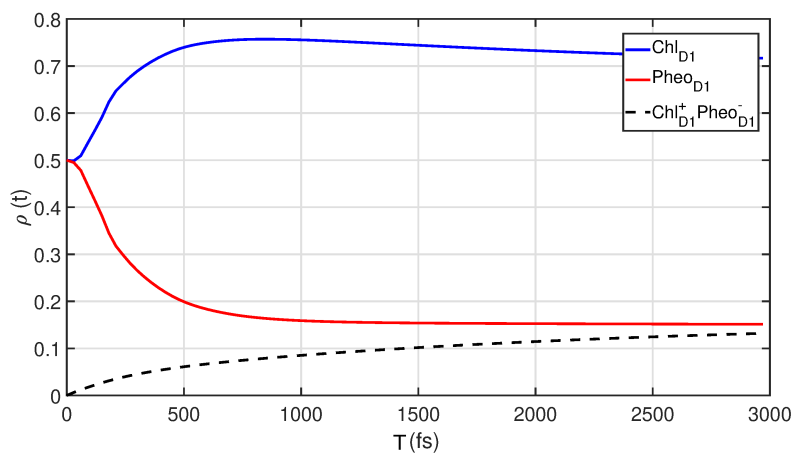


FIG. S18. Population dynamics of Chl_{D1} and Pheo_{D1} with the same parameters except the temperature ($T = 80$ K).

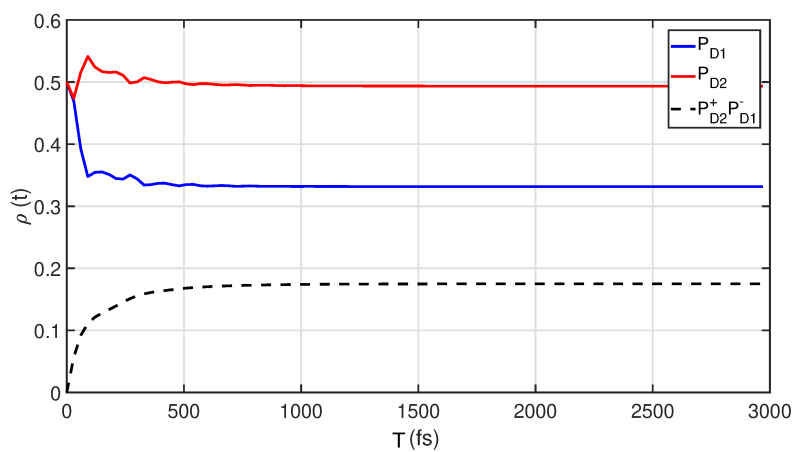


FIG. S19. Population dynamics of P_{D1} and P_{D1} at 80 K.

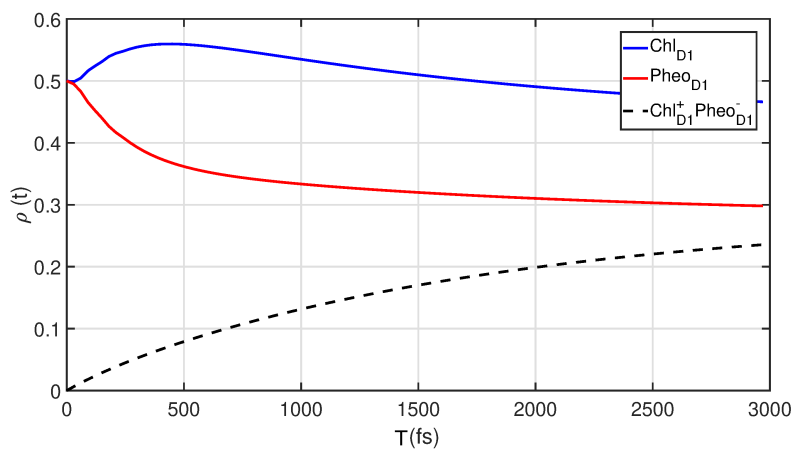


FIG. S20. Population dynamics of Chl_{D1} and Pheo_{D1} at 300 K.

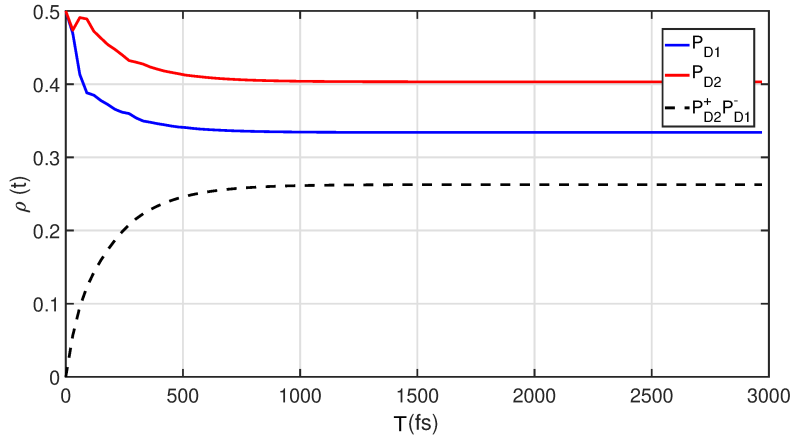


FIG. S21. Population dynamics of P_{D1} and P_{D2} at 300 K. The weak oscillatory dynamics of vibrational the coherence is present during the population dynamics of P_{D1} and P_{D2} .

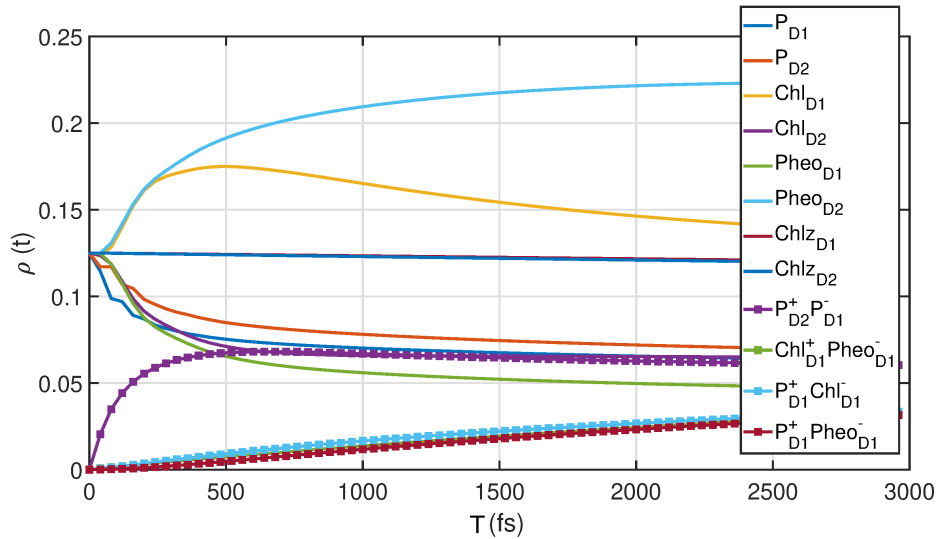


FIG. S22. Population dynamics of the PSII reaction center at 80 K. The population of the cofactors (charge-transfer states) are plotted as solid (square dotted) lines.

XVI. UNIQUENESS OF THE MODEL PARAMETERS AND COMPARISON

In this section, we address the uniqueness of our model and parameters and also compare to other results from Ref. 29, 30. For this, we take the parameters (site energies and electronic couplings) from Ref. 29, 30 and show the resulting calculated 2D electronic spectra (rephasing part) in Fig. S24. We show that, based on the modified Redfield quantum master equation, our model and parameters show the highest fitting quality. The results which we obtain from the model and parameters of Ref. 29 and 30 show slightly less accurate 2D spectra. This illustrates that the model developed here and the obtained parameters are a suitable approach to calculate 2D electronic spectra of the PSII reaction center at 20 K. Based on the modified Redfield quantum master equation and the calculations of response functions by the doorway-window method, we cannot completely rule out the models and parameters of other groups with advanced approaches of calculations. However, the calculations with numerically exact methods is commonly limited by computational resources. Thus, we employ in the next section the QUAPI approach for the calculations of the coherent dynamics in the PSII reaction center at low temperature (20 K), yet, with only the limited dimer model with a particular CT state involved.

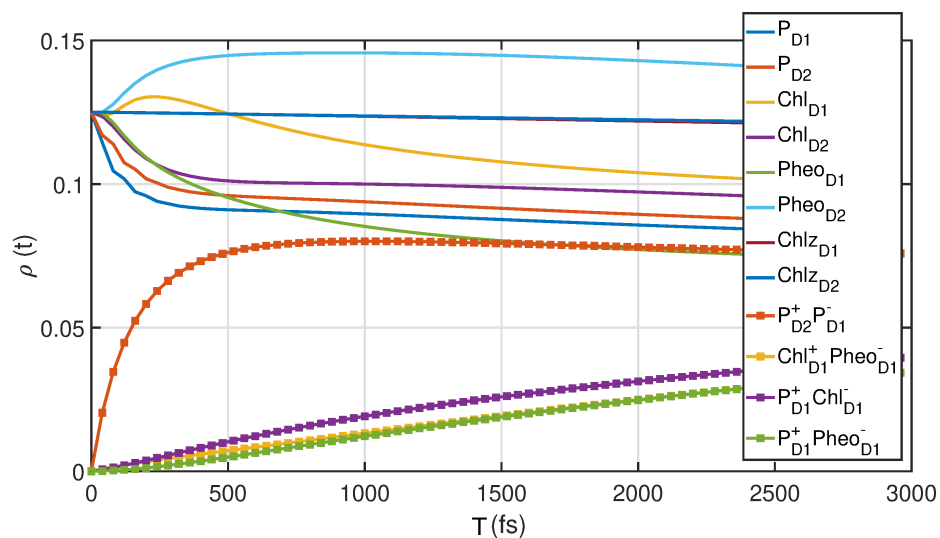


FIG. S23. Population dynamics of the PSII reaction center at 300 K. The population of cofactors (charge-transfer states) are plotted as solid (square dotted) lines.

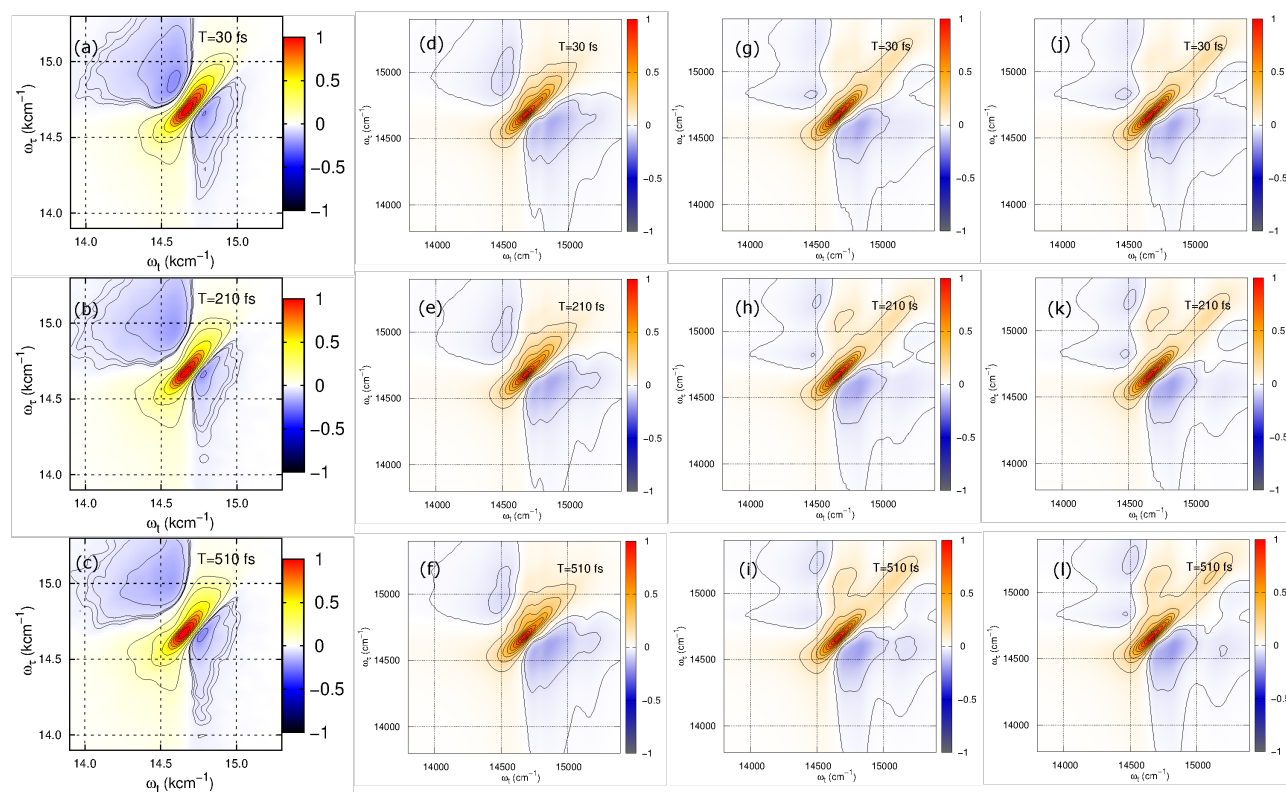


FIG. S24. Rephasing part of 2D electronic spectra of the measured (a) to (c) and calculated (d) to (l) data. The 2D electronic spectra from this study are shown from (d) to (f). The results from Ref. 30 are shown from (g) to (i). The calculated 2D spectra from Ref. 29 are presented from (j) to (l).

XVII. NUMERICALLY EXACT QUASI-ADIABATIC PATH INTEGRAL METHOD

In this section, we briefly summarize the quasi-adiabatic path integral (QUAPI) method. For simplicity, we assume that the interaction between the system and bath is switched on at $t = 0$, i. e., the initial density matrix has the form

$$\rho(0) = \rho_S(0)\rho_B(0). \quad (\text{S30})$$

Then, the evolution of the reduced density matrix of the system

$$\rho_S(s'', s', t) = \text{tr}_B \langle s'' | e^{-iHt/\hbar} \rho(0) e^{iHt/\hbar} | s' \rangle, \quad (\text{S31})$$

is given by

$$\begin{aligned} \rho_S(s'', s'; t) = & \int ds_0^+ \int ds_1^+ \cdots \int ds_{N-1}^+ \int ds_0^- \int ds_1^- \cdots \int ds_{N-1}^- \langle s'' | e^{-iH_0\Delta t/\hbar} | s_{N-1}^+ \rangle \cdots \langle s_1^+ | e^{-iH_0\Delta t/\hbar} | s_0^+ \rangle \\ & \times \langle s_0^+ | \rho_S(0) | s_0^- \rangle \langle s_0^- | e^{iH_0\Delta t/\hbar} | s_1^- \rangle \cdots \langle s_{N-1}^- | e^{iH_0\Delta t/\hbar} | s' \rangle I(s_0^+, s_1^+, \dots, s_{N-1}^+, s'', s_0^-, s_1^-, \dots, s_{N-1}^-, s'; \Delta t) \end{aligned} \quad (\text{S32})$$

where the time-discretized influence functional is

$$\begin{aligned} I(s_0^+, s_1^+, \dots, s_{N-1}^+, s'', s_0^-, s_1^-, \dots, s_{N-1}^-, s'; \Delta t) = & \text{tr}_B [e^{-iH_B(s'')\Delta t/2\hbar} e^{-iH_B(s_{N-1}^+)\Delta t/2\hbar} \\ & \times \dots e^{-iH_B(s_0^+)\Delta t/2\hbar} \rho_B(0) e^{-iH_B(s_0^-)\Delta t/2\hbar} \times \dots e^{-iH_B(s_{N-1}^-)\Delta t/2\hbar} e^{-iH_B(s')\Delta t/2\hbar}], \end{aligned} \quad (\text{S33})$$

which is taken from Ref. 43. Specifically, if the bath is initially at temperature $(k_B\beta)^{-1}$, the influence functional is given by

$$I = \exp\left\{-1/\hbar \sum_{k=0}^N \sum_{k'=0}^k (s_k^+ - s_k^-)(\eta_{kk'} s_{k'}^+ - \eta_{kk'}^* s_{k'}^-)\right\}. \quad (\text{S34})$$

The parameters $\eta_{kk'}$, $\eta_{kk'}^*$ are given by

$$\begin{aligned} \eta_{kk'} &= \frac{2}{\pi} \int_{-\infty}^{\infty} d\omega \frac{J(\omega)}{\omega^2} \frac{\exp(\beta\hbar\omega/2)}{\sinh(\beta\hbar\omega/2)} \sin^2(\omega\Delta t/2) e^{-i\omega\Delta t(k-k')}, 0 < k' < k < N, \\ \eta_{kk} &= \frac{1}{2\pi} \int_{-\infty}^{\infty} d\omega \frac{J(\omega)}{\omega^2} \frac{\exp(\beta\hbar\omega/2)}{\sinh(\beta\hbar\omega/2)} (1 - e^{-i\omega\Delta t}), 0 < k < N, \\ \eta_{N0} &= \frac{2}{\pi} \int_{-\infty}^{\infty} d\omega \frac{J(\omega)}{\omega^2} \frac{\exp(\beta\hbar\omega/2)}{\sinh(\beta\hbar\omega/2)} \sin^2(\omega\Delta t/4) e^{-i\omega(t-\Delta t/2)}, \\ \eta_{00} = \eta_{NN} &= \frac{1}{2\pi} \int_{-\infty}^{\infty} d\omega \frac{J(\omega)}{\omega^2} \frac{\exp(\beta\hbar\omega/2)}{\sinh(\beta\hbar\omega/2)} (1 - e^{-i\omega\Delta t/2}), \\ \eta_{k0} &= \frac{2}{\pi} \int_{-\infty}^{\infty} d\omega \frac{J(\omega)}{\omega^2} \frac{\exp(\beta\hbar\omega/2)}{\sinh(\beta\hbar\omega/2)} \sin(\omega\Delta t/4) \sin(\omega\Delta t/2) e^{-i\omega(k\Delta t-\Delta t/4)}, 0 < k < N, \\ \eta_{Nk} &= \frac{2}{\pi} \int_{-\infty}^{\infty} d\omega \frac{J(\omega)}{\omega^2} \frac{\exp(\beta\hbar\omega/2)}{\sinh(\beta\hbar\omega/2)} \sin(\omega\Delta t/4) \sin(\omega\Delta t/2) e^{-i\omega(t-k\Delta t-\Delta t/4)}, 0 < k < N, \end{aligned} \quad (\text{S35})$$

see Ref. 43, 44. The time propagation of QUAPI is performed by the reduced density tensor

$$T^{(2\Delta k_{max})}(s_k^\pm, s_{k+1}^\pm, \dots, s_{k+2\Delta k_{max}-1}^\pm)$$

and the propagator matrix $A^{\Delta k_{max}}$. Both are given by

$$\begin{aligned} A^{(\Delta k_{max})}(s_{k+\Delta k_{max}}^\pm, \dots, s_{k+2\Delta k_{max}-1}^\pm; (k + \Delta k_{max})\Delta t) = & \\ \int ds_k^\pm \cdots \int ds_{k+\Delta k_{max}-1}^\pm T^{(2\Delta k_{max})} \times (s_k^\pm, s_{k+1}^\pm, \dots, s_{k+2\Delta k_{max}-1}^\pm) A^{\Delta k_{max}} & \\ \times (s_k^\pm, \dots, s_{k+\Delta k_{max}-1}^\pm; k\Delta t) & \end{aligned} \quad (\text{S36})$$

and by

$$\begin{aligned} T^{(2\Delta k_{max})}(s_k^\pm, s_{k+1}^\pm, \dots, s_{k+2\Delta k_{max}-1}^\pm) = & \prod_{n=k}^{k+\Delta k_{max}-1} I_0(s_n^\pm) I_1(s_n^\pm) I_2(s_n^\pm, s_{n+2}^\pm) \\ & \times \dots I_{\Delta k_{max}}(s_n^\pm, s_{n+\Delta k_{max}}^\pm) K(s_n^\pm, s_{n+1}^\pm). \end{aligned} \quad (\text{S37})$$

The initial condition of the reduced density tensor can be expressed as

$$A^{(\Delta k_{max})}(s_0^\pm, s_1^\pm, \dots, s_{\Delta k_{max}}^\pm; 0) = \langle s_0^+ | \rho_s(0) | s_0^- \rangle. \quad (\text{S38})$$

Based on this iteration, we obtain the time-resolved density matrix of the system. The finite memory time of the system can be written as $\tau = \Delta k_{max} \Delta t$. The reduced density matrix at time $t = N \Delta t$ is given by

$$\rho_s(s_N^\pm; N \Delta t) = A^{(\Delta k_{max})}(s_N^\pm, s_{N+1}^\pm = \dots = s_{N+\Delta k_{max}-1}^\pm = 0; N \Delta t) I_0(s_N^\pm). \quad (\text{S39})$$

REFERENCES AND NOTES

1. Y. Umena, K. Kawakami, J.-R. Shen, N. Kamiya, Crystal structure of oxygen-evolving photosystem II at a resolution of 1.9 Å. *Nature* **473**, 55–60 (2011).
2. R. Dods, P. Båth, D. Morozov, V. A. Gagnér, D. Arnlund, H. L. Luk, J. Kübel, M. Maj, A. Vallejos, C. Wickstrand, R. Bosman, K. R. Beyerlein, G. Nelson, M. Liang, D. Milathianaki, J. Robinson, R. Harimoorthy, P. Berntsen, E. Malmerberg, L. Johansson, R. Andersson, S. Carbajo, E. Claesson, C. E. Conrad, P. Dahl, G. Hammarin, M. S. Hunter, C. Li, S. Lisova, A. Royant, C. Safari, A. Sharma, G. J. Williams, O. Yefanov, S. Westenhoff, J. Davidsson, D. P. De Ponte, S. Boutet, A. Barty, G. Katona, G. Groenhof, G. Brändén, R. Neutze, Ultrafast structural changes within a photosynthetic reaction centre. *Nature* **589**, 310–314 (2021).
3. M. Suga, F. Akita, K. Hirata, G. Ueno, H. Murakami, Y. Nakajima, T. Shimizu, K. Yamashita, M. Yamamoto, H. Ago, J.-R. Shen, Native structure of photosystem II at 1.95 Å resolution viewed by femtosecond X-ray pulses. *Nature* **517**, 99–103 (2015).
4. B. A. Diner, F. Rappaport, Structure, dynamics, and energetics of the primary photochemistry of photosystem II of oxygenic photosynthesis. *Annu. Rev. Plant Biol.* **53**, 551–580 (2002).
5. V. I. Novoderezhkin, E. G. Andrizhiyevskaya, J. P. Dekker, R. van Grondelle, Pathways and timescales of primary charge separation in the photosystem II reaction center as revealed by a simultaneous fit of time-resolved fluorescence and transient absorption. *Biophys. J.* **89**, 1464–1481 (2005).
6. V. I. Novoderezhkin, J. P. Dekker, R. van Grondelle, Mixing of exciton and charge-transfer states in photosystem II reaction centers: Modeling of stark spectra with modified redfield theory. *Biophys. J.* **93**, 1293–1311 (2007).
7. V. I. Prokhorenko, A. R. Holzwarth, Primary processes and structure of the Photosystem II reaction center: A photon echo study. *J. Phys. Chem. B* **104**, 11563–11578 (2000).
8. E. Romero, I. H. M. van Stokkum, V. I. Novoderezhkin, J. P. Dekker, R. van Grondelle, Two different charge separation pathways in Photosystem II. *Biochemistry* **49**, 4300–4307 (2010).
9. V. I. Novoderezhkin, E. Romero, J. P. Dekker, R. van Grondelle, Multiple Charge-separation pathways in photosystem II: Modeling of transient absorption kinetics. *Chemphyschem* **12**, 681–688 (2011).
10. G. S. Engel, T. R. Calhoun, E. L. Read, T.-K. Ahn, T. Mancal, Y.-C. Cheng, R. E. Blankenship, G. R. Fleming, Evidence for wavelike energy transfer through quantum coherence in photosynthetic systems. *Nature* **446**, 782–786 (2007).

11. E. Collini, C. Y. Wong, K. E. Wilk, P. M. G. Curmi, P. Brumer, G. D. Scholes, Coherently wired light-harvesting in photosynthetic marine algae at ambient temperature. *Nature* **463**, 644–647 (2010).
12. J. Cao, R. J. Cogdell, D. F. Coker, H.-G. Duan, J. Hauer, U. Kleinekathöfer, T. L. C. Jansen, T. Mančal, R. J. D. Miller, J. P. Ogilvie, V. I. Prokhorenko, T. Renger, H.-S. Tan, R. Tempelaar, M. Thorwart, E. Thyryhaug, S. Westenhoff, D. Zigmantas, Quantum biology revisited. *Sci. Adv.* **6**, eaaz4888 (2020).
13. H.-G. Duan, V. I. Prokhorenko, R. J. Cogdell, K. Ashraf, A. L. Stevens, M. Thorwart, R. J. D. Miller, Nature does not rely on long-lived electronic quantum coherence for photosynthetic energy transfer. *Proc. Natl. Acad. Sci. U.S.A.* **114**, 8493–8498 (2017).
14. G. D. Scholes, G. R. Fleming, L. X. Chen, A. Aspuru-Guzik, A. Buchleitner, D. F. Coker, G. S. Engel, R. van Grondelle, A. Ishizaki, D. M. Jonas, J. S. Lundeen, J. K. Mc Cusker, S. Mukamel, J. P. Ogilvie, A. Olaya-Castro, M. A. Ratner, F. C. Spano, K. Birgitta Whaley, X. Zhu, Using coherence to enhance function in chemical and biophysical systems. *Nature* **543**, 647–656 (2017).
15. E. Thyryhaug, R. Tempelaar, M. J. P. Alcocer, Karel Židek, D. Bína, J. Knoester, T. L. C. Jansen, D. Zigmantas, Identification and characterization of diverse coherences in the Fenna–Matthews–Olson complex. *Nat. Chem.* **10**, 780–786 (2018).
16. H.-G. Duan, A. Jha, L. Chen, V. Tiwari, R. J. Cogdell, K. Ashraf, V. I. Prokhorenko, M. Thorwart, R. J. D. Miller, Quantum coherent energy transport in the Fenna–Matthews–Olson complex at low temperature. *Proc. Natl. Acad. Sci. U.S.A.* **119**, e2212630119 (2022).
17. L. Wang, M. A. Allodi, G. S. Engel, Quantum coherences reveal excited-state dynamics in biophysical systems. *Nat. Rev. Chem.* **3**, 477–490 (2019).
18. E. Romero, V. I. Novoderezhkin, R. van Grondelle, Quantum design of photosynthesis for bio-inspired solar-energy conversion. *Nature* **543**, 355–365 (2017).
19. V. Tiwari, W. K. Peters, D. M. Jonas, Electronic resonance with anticorrelated pigment vibrations drives photosynthetic energy transfer outside the adiabatic framework. *Proc. Natl. Acad. Sci. U.S.A.* **110**, 1203–1208 (2013).
20. A. W. Chin, J. Prior, R. Rosenbach, F. Caycedo-Soler, S. F. Huelga, M. B. Plenio, The role of non-equilibrium vibrational structures in electronic coherence and recoherence in pigment–protein complexes. *Nat. Phys.* **9**, 113–118 (2013).
21. A. Halpin, P. J. M. Johnson, R. Tempelaar, R. S. Murphy, J. Knoester, T. L. C. Jansen, R. J. D. Miller, Two-dimensional spectroscopy of a molecular dimer unveils the effects of vibronic coupling on exciton coherences. *Nat. Chem.* **6**, 196–201 (2014).

22. H.-G. Duan, P. Nalbach, V. I. Prokhorenko, S. Mukamel, M. Thorwart, On the origin of oscillations in two-dimensional spectra of excitonically-coupled molecular systems. *New J. Phys.* **17**, 072002 (2015).
23. C. Kreisbeck, T. Kramer Long-lived electronic coherence in dissipative exciton dynamics of light-harvesting complexes. *J. Phys. Chem. Lett.* **3**, 2828–2833 (2012).
24. D. Egorova Self-analysis of coherent oscillations in time-resolved optical signals. *J. Phys. Chem. A* **118**, 10259–10267 (2014).
25. F. Milota, V. I. Prokhorenko, T. Mancal, H. von Berlepsch, O. Bixner, H. F. Kauffmann, J. Hauer, vibronic and vibrational coherences in two-dimensional electronic spectra of supramolecular J-aggregates. *J. Phys. Chem. A* **117**, 6007–6014 (2013).
26. J. A. Myers, K. L. M. Lewis, F. D. Fuller, P. F. Tekavec, C. F. Yocum, J. P. Ogilvie, Two-dimensional electronic spectroscopy of the D1-D2-cyt b559 photosystem II reaction Center complex. *J. Phys. Chem. Lett.* **1**, 2774–2780 (2010).
27. K. L. M. Lewis, F. D. Fuller, J. A. Myers, C. F. Yocum, S. Mukamel, D. Abramavicius, J. P. Ogilvie, Simulations of the two-dimensional electronic spectroscopy of the photosystem II reaction center. *J. Phys. Chem. A* **117**, 34–41 (2013).
28. A. Gelzinis, L. Valkunas, F. D. Fuller, J. P. Ogilvie, S. Mukamel, D. Abramavicius, Tight-binding model of the photosystem II reaction center: Application to two-dimensional electronic spectroscopy. *New J. Phys.* **15**, 075013 (2013).
29. E. Romero, R. Augulis, V. I. Novoderezhkin, M. Ferretti, J. Thieme, D. Zigmantas, R. van Grondelle, Quantum coherence in photosynthesis for efficient solar-energy conversion. *Nat. Phys.* **10**, 676–682 (2014).
30. F. D. Fuller, J. Pan, A. Gelzinis, V. Butkus, S. Seckin Senlik, D. E. Wilcox, C. F. Yocum, L. Valkunas, D. Abramavicius, J. P. Ogilvie, Vibronic coherence in oxygenic photosynthesis. *Nat. Chem.* **6**, 706–711 (2014).
31. Y. Yoneda, E. A. Arsenault, S.-J. Yang, K. Orcutt, M. Iwai, G. R. Fleming, The initial charge separation step in oxygenic photosynthesis. *Nat. Commun.* **13**, 2275 (2022).
32. H. H. Nguyen, Y. Song, E. L. Maret, Y. Silori, R. Willow, C. F. Yocum, J. P. Ogilvie, Charge separation in the photosystem II reaction center resolved by multispectral two-dimensional electronic spectroscopy. *Sci. Adv.* **9**, eade7190 (2023).
33. V. I. Prokhorenko, “Global analysis of multi-dimensional experimental data,” *European Photochemistry Association Newsletter*, June 2012, pp. 21–23.

34. H.-G. Duan, A. L. Stevens, P. Nalbach, M. Thorwart, V. I. Prokhorenko, R. J. D. Miller, Two-dimensional electronic spectroscopy of light-harvesting complex II at ambient temperature: A joint experimental and theoretical study. *J. Phys. Chem. B* **119**, 12017–12027 (2015).
35. H.-G. Duan, V. I. Prokhorenko, E. Wientjes, R. Croce, M. Thorwart, R. J. D. Miller, Primary charge separation in the photosystem II reaction center revealed by a global analysis of the two-dimensional electronic spectra. *Sci. Rep.* **7**, 12347 (2017).
36. E. J. G. Peterman, H. van Amerongen, R. van Grondelle, J. P. Dekker, The nature of the excited state of the reaction center of photosystem II of green plants: A high-resolution fluorescence spectroscopy study. *Proc. Natl. Acad. Sci. U.S.A.* **95**, 6128–6133 (1998).
37. V. Butkus, D. Zigmantas, L. Valkunas, D. Abramavicius, Vibrational vs. electronic coherences in 2D spectrum of molecular systems. *Chem. Phys. Lett.* **545**, 40–43 (2012).
38. V. Butkus, L. Valkunas, D. Abramavicius, Vibronic phenomena and exciton–vibrational interference in two-dimensional spectra of molecular aggregates. *J. Chem. Phys.* **140**, 034306 (2014).
39. H.-G. Duan, A. G. Dijkstra, P. Nalbach, M. Thorwart, Efficient tool to calculate two-dimensional optical spectra for photoactive molecular complexes. *Phys. Rev. E Stat. Nonlin. Soft Matter Phys.* **92**, 042708 (2015).
40. M. Yang, G. R. Fleming, Influence of phonons on exciton transfer dynamics: Comparison of the Redfield, Förster, and modified Redfield equations. *Chem. Phys.* **282**, 163–180 (2002).
41. W. M. Zhang, T. Meier, V. Chernyak, S. Mukamel, Exciton-migration and three-pulse femtosecond optical spectroscopies of photosynthetic antenna complexes. *J. Chem. Phys.* **108**, 7763–7774 (1998).
42. C. Olbrich, T. L. C. Jansen, J. Liebers, M. Aghtar, J. Strümpfer, K. Schulten, J. Knoester, U. Kleinekathöfer, From atomistic modeling to excitation transfer and two-dimensional spectra of the FMO light-harvesting complex. *J. Phys. Chem. B* **115**, 8609–8621 (2011).
43. N. Makri, D. E. Makarov Tensor propagator for iterative quantum time evolution of reduced density matrices. I. Theory. *J. Chem. Phys.* **102**, 4600–4610 (1995).
44. N. Makri, D. E. Makarov Tensor propagator for iterative quantum time evolution of reduced density matrices II. Numerical methodology. *J. Chem. Phys.* **102**, 4611–4618 (1995).
45. P. Nalbach, D. Braun, M. Thorwart Exciton transfer dynamics and quantumness of energy transfer in the Fenna-Matthews-Olson complex. *Phys. Rev. E* **84**, 041926 (2011).
46. S. Caffarri, R. Kouril, S. Kereiche, E. J. Boekema, R. Croce, Functional architecture of higher plant photosystem II supercomplexes. *EMBO J.* **28**, 3052–3063 (2009).

47. S. Caffarri, R. Croce, L. Cattivelli, R. Bassi, A look within LHCII: Differential Analysis of the Lhcb1–3 complexes building the major trimeric antenna complex of higher-plant photosynthesis. *Biochemistry* **43**, 9467–9476 (2004).
48. D. A. Berthold, G. T. Babcock, C. F. Yocum, A highly resolved, oxygen-evolving photosystem II preparation from spinach thylakoid membranes. *FEBS Lett.* **134**, 231–234 (1981).
49. P. J. van Leeuwen, M. C. Nieveen, E. J. van de Meent, J. P. Dekker, H. J. van Gorkom, Rapid and simple isolation of pure photosystem II core and reaction center particles from spinach. *Photosynth. Res.* **28**, 149–153 (1991).
50. C. Eijkelhoff, J. P. Dekker, A routine method to determine the chlorophyll a, pheophytin a and β -carotene contents of isolated Photosystem II reaction center complexes. *Photosynth. Res.* **52**, 69–73 (1997).
51. S. L. S. Kwa, W. R. Newell, R. van Grondelle, J. P. Dekker, The reaction center of photosystem II studied with polarized fluorescence spectroscopy. *Biochim. Biophys. Acta* **1099**, 193–202 (1992).
52. J. D. Hybl, A. A. Ferro, D. M. Jonas, Two-dimensional Fourier transform electronic spectroscopy. *J. Chem. Phys.* **115**, 6606–6622 (2001).
53. M. Schröder, U. Kleinekathöfer, M. Schreiber, Calculation of absorption spectra for light-harvesting systems using non-Markovian approaches as well as modified Redfield theory. *J. Chem. Phys.* **124**, 084903 (2006).
54. A. Ishizaki, G. R. Fleming, On the adequacy of the Redfield equation and related approaches to the study of quantum dynamics in electronic energy transfer. *J. Chem. Phys.* **130**, 234110 (2009).
55. M. Schröder, M. Schreiber, U. Kleinekathöfer, A time-dependent modified Redfield theory for absorption spectra applied to light-harvesting systems. *J. Lumin.* **125**, 126–132 (2007).
56. V. May, O. Kuhn, *Charge and Energy Transfer Dynamics in Molecular Systems* (Wiley-VCH Press, 2011).
57. R. P. Feynman, F. L. Vernon Jr., The theory of a general quantum system interacting with a linear dissipative system. *Ann. Phys.* **24**, 118–173 (1963).

REFERENCES

1. Y. Umena, K. Kawakami, J.-R. Shen, N. Kamiya, Crystal structure of oxygen-evolving photosystem II at a resolution of 1.9 Å. *Nature* **473**, 55–60 (2011).
2. R. Dods, P. Båth, D. Morozov, V. A. Gagnér, D. Arnlund, H. L. Luk, J. Kübel, M. Maj, A. Vallejos, C. Wickstrand, R. Bosman, K. R. Beyerlein, G. Nelson, M. Liang, D. Milathianaki, J. Robinson, R. Harimoorthy, P. Berntsen, E. Malmerberg, L. Johansson, R. Andersson, S. Carbajo, E. Claesson, C. E. Conrad, P. Dahl, G. Hammarin, M. S. Hunter, C. Li, S. Lisova, A. Royant, C. Safari, A. Sharma, G. J. Williams, O. Yefanov, S. Westenhoff, J. Davidsson, D. P. De Ponte, S. Boutet, A. Barty, G. Katona, G. Groenhof, G. Brändén, R. Neutze, Ultrafast structural changes within a photosynthetic reaction centre. *Nature* **589**, 310–314 (2021).
3. M. Suga, F. Akita, K. Hirata, G. Ueno, H. Murakami, Y. Nakajima, T. Shimizu, K. Yamashita, M. Yamamoto, H. Ago, J.-R. Shen, Native structure of photosystem II at 1.95 Å resolution viewed by femtosecond X-ray pulses. *Nature* **517**, 99–103 (2015).
4. B. A. Diner, F. Rappaport, Structure, dynamics, and energetics of the primary photochemistry of photosystem II of oxygenic photosynthesis. *Annu. Rev. Plant Biol.* **53**, 551–580 (2002).
5. V. I. Novoderezhkin, E. G. Andrizhiyevskaya, J. P. Dekker, R. van Grondelle, Pathways and timescales of primary charge separation in the photosystem II reaction center as revealed by a simultaneous fit of time-resolved fluorescence and transient absorption. *Biophys. J.* **89**, 1464–1481 (2005).
6. V. I. Novoderezhkin, J. P. Dekker, R. van Grondelle, Mixing of exciton and charge-transfer states in photosystem II reaction centers: Modeling of stark spectra with modified redfield theory. *Biophys. J.* **93**, 1293–1311 (2007).
7. V. I. Prokhorenko, A. R. Holzwarth, Primary processes and structure of the Photosystem II reaction center: A photon echo study. *J. Phys. Chem. B* **104**, 11563–11578 (2000).
8. E. Romero, I. H. M. van Stokkum, V. I. Novoderezhkin, J. P. Dekker, R. van Grondelle, Two different charge separation pathways in Photosystem II. *Biochemistry* **49**, 4300–4307 (2010).
9. V. I. Novoderezhkin, E. Romero, J. P. Dekker, R. van Grondelle, Multiple Charge-separation pathways in photosystem II: Modeling of transient absorption kinetics. *Chemphyschem* **12**, 681–688 (2011).
10. G. S. Engel, T. R. Calhoun, E. L. Read, T.-K. Ahn, T. Mancal, Y.-C. Cheng, R. E. Blankenship, G. R. Fleming, Evidence for wavelike energy transfer through quantum coherence in photosynthetic systems. *Nature* **446**, 782–786 (2007).

11. E. Collini, C. Y. Wong, K. E. Wilk, P. M. G. Curmi, P. Brumer, G. D. Scholes, Coherently wired light-harvesting in photosynthetic marine algae at ambient temperature. *Nature* **463**, 644–647 (2010).
12. J. Cao, R. J. Cogdell, D. F. Coker, H.-G. Duan, J. Hauer, U. Kleinekathöfer, T. L. C. Jansen, T. Mančal, R. J. D. Miller, J. P. Ogilvie, V. I. Prokhorenko, T. Renger, H.-S. Tan, R. Tempelaar, M. Thorwart, E. Thyryhaug, S. Westenhoff, D. Zigmantas, Quantum biology revisited. *Sci. Adv.* **6**, eaaz4888f (2020).
13. H.-G. Duan, V. I. Prokhorenko, R. J. Cogdell, K. Ashraf, A. L. Stevens, M. Thorwart, R. J. D. Miller, Nature does not rely on long-lived electronic quantum coherence for photosynthetic energy transfer. *Proc. Natl. Acad. Sci. U.S.A.* **114**, 8493–8498 (2017).
14. G. D. Scholes, G. R. Fleming, L. X. Chen, A. Aspuru-Guzik, A. Buchleitner, D. F. Coker, G. S. Engel, R. van Grondelle, A. Ishizaki, D. M. Jonas, J. S. Lundeen, J. K. Mc Cusker, S. Mukamel, J. P. Ogilvie, A. Olaya-Castro, M. A. Ratner, F. C. Spano, K. Birgitta Whaley, X. Zhu, Using coherence to enhance function in chemical and biophysical systems. *Nature* **543**, 647–656 (2017).
15. E. Thyryhaug, R. Tempelaar, M. J. P. Alcocer, Karel Židek, D. Bína, J. Knoester, T. L. C. Jansen, D. Zigmantas, Identification and characterization of diverse coherences in the Fenna–Matthews–Olson complex. *Nat. Chem.* **10**, 780–786 (2018).
16. H.-G. Duan, A. Jha, L. Chen, V. Tiwari, R. J. Cogdell, K. Ashraf, V. I. Prokhorenko, M. Thorwart, R. J. D. Miller, Quantum coherent energy transport in the Fenna–Matthews–Olson complex at low temperature. *Proc. Natl. Acad. Sci. U.S.A.* **119**, e2212630119 (2022).
17. L. Wang, M. A. Allodi, G. S. Engel, Quantum coherences reveal excited-state dynamics in biophysical systems. *Nat. Rev. Chem.* **3**, 477–490 (2019).
18. E. Romero, V. I. Novoderezhkin, R. van Grondelle, Quantum design of photosynthesis for bio-inspired solar-energy conversion. *Nature* **543**, 355–365 (2017).
19. V. Tiwari, W. K. Peters, D. M. Jonas, Electronic resonance with anticorrelated pigment vibrations drives photosynthetic energy transfer outside the adiabatic framework. *Proc. Natl. Acad. Sci. U.S.A.* **110**, 1203–1208 (2013).
20. A. W. Chin, J. Prior, R. Rosenbach, F. Caycedo-Soler, S. F. Huelga, M. B. Plenio, The role of non-equilibrium vibrational structures in electronic coherence and recoherence in pigment–protein complexes. *Nat. Phys.* **9**, 113–118 (2013).
21. A. Halpin, P. J. M. Johnson, R. Tempelaar, R. S. Murphy, J. Knoester, T. L. C. Jansen, R. J. D. Miller, Two-dimensional spectroscopy of a molecular dimer unveils the effects of vibronic coupling on exciton coherences. *Nat. Chem.* **6**, 196–201 (2014).

22. H.-G. Duan, P. Nalbach, V. I. Prokhorenko, S. Mukamel, M. Thorwart, On the origin of oscillations in two-dimensional spectra of excitonically-coupled molecular systems. *New J. Phys.* **17**, 072002 (2015).
23. C. Kreisbeck, T. Kramer Long-lived electronic coherence in dissipative exciton dynamics of light-harvesting complexes. *J. Phys. Chem. Lett.* **3**, 2828–2833 (2012).
24. V. Butkus, D. Zigmantas, L. Valkunas, D. Abramavicius, Vibrational vs. electronic coherences in 2D spectrum of molecular systems. *Chem. Phys. Lett.* **545**, 40–43 (2012).
25. V. Butkus, L. Valkunas, D. Abramavicius, Vibronic phenomena and exciton–vibrational interference in two-dimensional spectra of molecular aggregates. *J. Chem. Phys.* **140**, 034306 (2014).
26. D. Egorova Self-analysis of coherent oscillations in time-resolved optical signals. *J. Phys. Chem. A* **118**, 10259–10267 (2014).
27. F. Milota, V. I. Prokhorenko, T. Mancal, H. von Berlepsch, O. Bixner, H. F. Kauffmann, J. Hauer, vibronic and vibrational coherences in two-dimensional electronic spectra of supramolecular J-aggregates. *J. Phys. Chem. A* **117**, 6007–6014 (2013).
28. J. A. Myers, K. L. M. Lewis, F. D. Fuller, P. F. Tekavec, C. F. Yocum, J. P. Ogilvie, Two-dimensional electronic spectroscopy of the D1-D2-cyt b559 photosystem II reaction Center complex. *J. Phys. Chem. Lett.* **1**, 2774–2780 (2010).
29. K. L. M. Lewis, F. D. Fuller, J. A. Myers, C. F. Yocum, S. Mukamel, D. Abramavicius, J. P. Ogilvie, Simulations of the two-dimensional electronic spectroscopy of the photosystem II reaction center. *J. Phys. Chem. A* **117**, 34–41 (2013).
30. A. Gelzinis, L. Valkunas, F. D. Fuller, J. P. Ogilvie, S. Mukamel, D. Abramavicius, Tight-binding model of the photosystem II reaction center: Application to two-dimensional electronic spectroscopy. *New J. Phys.* **15**, 075013 (2013).
31. E. Romero, R. Augulis, V. I. Novoderezhkin, M. Ferretti, J. Thieme, D. Zigmantas, R. van Grondelle, Quantum coherence in photosynthesis for efficient solar-energy conversion. *Nat. Phys.* **10**, 676–682 (2014).
32. H. H. Nguyen, Y. Song, E. L. Maret, Y. Silori, R. Willow, C. F. Yocum, J. P. Ogilvie, Charge separation in the photosystem II reaction center resolved by multispectral two-dimensional electronic spectroscopy. *Sci. Adv.* **9**, eade7190 (2023).
33. Y. Yoneda, E. A. Arsenault, S.-J. Yang, K. Orcutt, M. Iwai, G. R. Fleming, The initial charge separation step in oxygenic photosynthesis. *Nat. Commun.* **13**, 2275 (2022).

34. F. D. Fuller, J. Pan, A. Gelzinis, V. Butkus, S. Seckin Senlik, D. E. Wilcox, C. F. Yocum, L. Valkunas, D. Abramavicius, J. P. Ogilvie, Vibronic coherence in oxygenic photosynthesis. *Nat. Chem.* **6**, 706–711 (2014).
35. V. I. Prokhorenko, “Global analysis of multi-dimensional experimental data,” *European Photochemistry Association Newsletter*, June 2012, pp. 21–23.
36. H.-G. Duan, A. L. Stevens, P. Nalbach, M. Thorwart, V. I. Prokhorenko, R. J. D. Miller, Two-dimensional electronic spectroscopy of light-harvesting complex II at ambient temperature: A joint experimental and theoretical study. *J. Phys. Chem. B* **119**, 12017–12027 (2015).
37. H.-G. Duan, V. I. Prokhorenko, E. Wientjes, R. Croce, M. Thorwart, R. J. D. Miller, Primary charge separation in the photosystem II reaction center revealed by a global analysis of the two-dimensional electronic spectra. *Sci. Rep.* **7**, 12347 (2017).
38. E. J. G. Peterman, H. van Amerongen, R. van Grondelle, J. P. Dekker, The nature of the excited state of the reaction center of photosystem II of green plants: A high-resolution fluorescence spectroscopy study. *Proc. Natl. Acad. Sci. U.S.A.* **95**, 6128–6133 (1998).
39. H.-G. Duan, A. G. Dijkstra, P. Nalbach, M. Thorwart, Efficient tool to calculate two-dimensional optical spectra for photoactive molecular complexes. *Phys. Rev. E Stat. Nonlin. Soft Matter Phys.* **92**, 042708 (2015).
40. M. Yang, G. R. Fleming, Influence of phonons on exciton transfer dynamics: Comparison of the Redfield, Förster, and modified Redfield equations. *Chem. Phys.* **282**, 163–180 (2002).
41. W. M. Zhang, T. Meier, V. Chernyak, S. Mukamel, Exciton-migration and three-pulse femtosecond optical spectroscopies of photosynthetic antenna complexes. *J. Chem. Phys.* **108**, 7763–7774 (1998).
42. C. Olbrich, T. L. C. Jansen, J. Liebers, M. Aghtar, J. Strümpfer, K. Schulten, J. Knoester, U. Kleinekathöfer, From atomistic modeling to excitation transfer and two-dimensional spectra of the FMO light-harvesting complex. *J. Phys. Chem. B* **115**, 8609–8621 (2011).
43. N. Makri, D. E. Makarov Tensor propagator for iterative quantum time evolution of reduced density matrices. I. Theory. *J. Chem. Phys.* **102**, 4600–4610 (1995).
44. N. Makri, D. E. Makarov Tensor propagator for iterative quantum time evolution of reduced density matrices II. Numerical methodology. *J. Chem. Phys.* **102**, 4611–4618 (1995).
45. P. Nalbach, D. Braun, M. Thorwart Exciton transfer dynamics and quantumness of energy transfer in the Fenna-Matthews-Olson complex. *Phys. Rev. E* **84**, 041926 (2011).

46. S. Caffarri, R. Kouril, S. Kereïche, E. J. Boekema, R. Croce, Functional architecture of higher plant photosystem II supercomplexes. *EMBO J.* **28**, 3052–3063 (2009).
47. S. Caffarri, R. Croce, L. Cattivelli, R. Bassi, A look within LHCII: Differential Analysis of the Lhcb1–3 complexes building the major trimeric antenna complex of higher-plant photosynthesis. *Biochemistry* **43**, 9467–9476 (2004).
48. D. A. Berthold, G. T. Babcock, C. F. Yocum, A highly resolved, oxygen-evolving photosystem II preparation from spinach thylakoid membranes. *FEBS Lett.* **134**, 231–234 (1981).
49. P. J. van Leeuwen, M. C. Nieveen, E. J. van de Meent, J. P. Dekker, H. J. van Gorkom, Rapid and simple isolation of pure photosystem II core and reaction center particles from spinach. *Photosynth. Res.* **28**, 149–153 (1991).
50. C. Eijkelhoff, J. P. Dekker, A routine method to determine the chlorophyll a, pheophytin a and β -carotene contents of isolated Photosystem II reaction center complexes. *Photosynth. Res.* **52**, 69–73 (1997).
51. S. L. S. Kwa, W. R. Newell, R. van Grondelle, J. P. Dekker, The reaction center of photosystem II studied with polarized fluorescence spectroscopy. *Biochim. Biophys. Acta* **1099**, 193–202 (1992).
52. J. D. Hybl, A. A. Ferro, D. M. Jonas, Two-dimensional Fourier transform electronic spectroscopy. *J. Chem. Phys.* **115**, 6606–6622 (2001).
53. Y. Umena, K. Kawakami, J.-R. Shen, N. Kamiya, Crystal structure of oxygen-evolving photosystem II at a resolution of 1.9 Å. *Nature* **473**, 55–60 (2011).
54. V. I. Prokhorenko, *European Photochemistry Association Newsletter*, June 2012, p. 21.
55. V. Butkus, D. Zigmantas, L. Valkunas, D. Abramavicius, Vibrational vs. electronic coherences in 2D spectrum of molecular systems. *Chem. Phys. Lett.* **545**, 40–43 (2012).
56. M. Schröder, U. Kleinekathöfer, M. Schreiber, Calculation of absorption spectra for light-harvesting systems using non-Markovian approaches as well as modified Redfield theory. *J. Chem. Phys.* **124**, 084903 (2006).
57. A. Ishizaki, G. R. Fleming, On the adequacy of the Redfield equation and related approaches to the study of quantum dynamics in electronic energy transfer. *J. Chem. Phys.* **130**, 234110 (2009).
58. C. Meier, D. J. Tannor, Non-Markovian evolution of the density operator in the presence of strong laser fields. *J. Chem. Phys.* **111**, 3365–3376 (1999).
59. M. Schröder, M. Schreiber, U. Kleinekathöfer, A time-dependent modified Redfield theory for absorption spectra applied to light-harvesting systems. *J. Lumin.* **125**, 126–132 (2007).

60. V. May, O. Kuhn, *Charge and Energy Transfer Dynamics in Molecular Systems* (Wiley-VCH Press, 2011).
61. R. P. Feynman, F. L. Vernon Jr., The theory of a general quantum system interacting with a linear dissipative system. *Ann. Phys.* **24**, 118–173 (1963).